



Alexander Stoll

Optimisation of Nb/Al-AlO_x/Nb Tri-Layer
Deposition for Cross-Type Josephson Junction
Fabrication in the PreVAC Sputtering System

Master's thesis

June 2023

Faculty of Physics and Astronomy
Ruprecht-Karls-University Heidelberg

MASTER'S THESIS

in Physics

submitted by

Alexander Stoll

born in Buchen

June 2023

Optimisation of Nb/Al-AlO_x/Nb Tri-Layer Deposition for Cross-Type Josephson Junction Fabrication in the PreVAC Sputtering System

This Master thesis was carried out by Alexander Stoll
at the Kirchhoff-Institute for Physics
under the supervision of
Prof. Dr. C. Enss

This thesis discusses the optimisation of the Nb/Al-AlO_x/Nb tri-layer deposition for the fabrication of cross-type based Josephson tunnel junctions. Josephson tunnel junctions (JJs) are the core elements of various superconducting devices such as qubits or superconducting quantum interference devices (SQUIDs). The cross-type JJ geometry is motivated by the reduction of the junction area as well as parasitic capacities compared to the commonly used window-type geometry. The cross-like design removes parasitic effects with the additional benefit of simple and time efficient fabrication steps and relaxed alignment requirements during micro-fabrication. To ensure a reliable wafer-scale fabrication that yields JJs with a reproducible and uniform high quality, the in-house sputter-deposited niobium layers in a new sputtering system had to be investigated regarding their physical properties including the measurement of the critical temperature T_c , the stress of the niobium film and junction specific quality features. The parameters for the magnetron sputtering, like the Ar pressure and power of the sputtering source, were optimised accordingly. This resulted in the successful fabrication of high quality cross-type JJs with reduced area sizes by at least a factor 4 and homogeneously distributed quality parameters on wafer-scale, which provides a basis for further developments of cross-type based dc-SQUIDs.

Optimierung der Deponierung von Nb/Al-AlO_x/Nb Dreischichtstrukturen im PreVAC Sputter-System für die Fabrikation von Josephson Kreuztyp-Kontakten

In der vorliegenden Arbeit werden die durchgeführten Methoden zur Optimierung der Nb/Al-AlO_x/Nb Dreischicht-Deponierung für die Herstellung von Josephson-Tunnelkontakte auf Basis einer kreuzförmigen Geometrie vorgestellt. Josephson-Tunnelkontakte (JJs) sind die Kernelemente verschiedener supraleitender elektronischer Bauelemente. Die Verwendung der kreuzförmigen JJ-Geometrie ist durch die Verringerung der Kontaktfläche sowie der parasitären Kapazitäten im Vergleich zu der üblicherweise verwendeten Fenstertyp-Geometrie motiviert. Das kreuzförmige Design beseitigt parasitäre Effekte und bietet zudem den Vorteil einfacher und zeitsparender Herstellungsschritte. Um eine zuverlässige Fabrikation auf Wafer-Skala zu gewährleisten, die JJs mit reproduzierbarer und homogen hoher Qualität liefert, mussten die in dem neuen institutsinternen Sputtersystem deponierten Niobschichten auf ihre physikalischen Eigenschaften hin untersucht werden, einschließlich der Messung der kritischen Temperatur T_c , der Verspannung des Niobfilms und der JJ-spezifischen Qualitätsmerkmale. Die Parameter für das Magnetron-Sputtern, wie der Ar-Druck und die Leistung der Sputterquelle, wurden entsprechend optimiert. Dies führte zur erfolgreichen Herstellung von qualitativ hochwertigen Kreuztyp-Kontakten mit einer um mindestens den Faktor 4 reduzierten Flächengröße und homogen verteilten Qualitätsparametern auf Wafer-Skala, was eine Grundlage für weitere Entwicklungen von Kreuztyp-Kontakt basierten dc-SQUIDs liefert.

Contents

1	Introduction	1
2	Theoretical Background	3
2.1	Superconductivity	3
2.1.1	Quantization of Flux	5
2.2	Josephson Junction	6
2.2.1	Josephson Effect	6
2.2.2	Short Josephson Junctions	8
2.2.3	RCSJ Model	10
2.3	Quality Criteria for Josephson Junctions	15
2.3.1	Gap Voltage V_{gap}	16
2.3.2	$I_c R_n$ Product	17
2.3.3	Subgap Resistance R_{sg}	18
2.4	dc-SQUIDs	18
2.4.1	Zero Voltage State	19
2.4.2	Voltage state	21
2.4.3	Optimal Parameters	22
2.5	Unshunted dc-SQUIDs	25
3	Experimental Methods and Results	29
3.1	Fabrication Process of Nb/Al-AlO _x /Nb Junctions	29
3.1.1	Capacitance of Josephson Junctions	29
3.1.2	Window-type Josephson Junction	30
3.1.3	Cross-type Josephson Junction	32
3.1.4	Facilities at Kirchhoff-Institute for Physics	34

3.2 Optimisation of Trilayer Deposition	36
3.2.1 Stress Measurement	36
3.2.2 Minimizing Nb Film Stress	37
3.2.3 Aluminium Thickness and Oxidation	40
3.3 Characterisation of Josephson Junctions	42
3.3.1 Four-wire Sensing	42
3.3.2 Critical Current Determination	44
4 Cross-type Nb/Al-AlO_x/Nb Josephson Tunnel Junctions	47
4.1 Josephson Tunnel Junctions with 7 nm Aluminium and with 10 nm Aluminium	48
4.2 Josephson Tunnel Junctions With 14 nm Aluminium	50
4.3 Estimating the Capacitance of Josephson Junctions	54
5 Summary and Outlook	57
I Appendix	61
Bibliography	63

1. Introduction

High resolution particle detectors play a vital role in the frontier of discovering new physical phenomena and experimentally confirming current theories or driving the development of various models [Alp15, Gas17]. One successful realization of such high resolution detectors are metallic magnetic calorimeters (MMC) which are used as low temperature particle detectors [Fle05, Kem18]. The working principle of MMCs is based on the energy transfer of an incoming particle onto the absorber material causing a temperature change, which changes the magnetisation of a paramagnetic temperature sensor. This change in form of magnetic flux change is read out with a superconducting quantum interference device (SQUID). SQUIDs represent the state of the art technology in precision measurements of magnetic flux changes with high bandwidth. A SQUID consists of a superconducting loop with either one Josephson tunnel junction (JJ), the rf-SQUID, or two JJs, the dc-SQUID, interrupting this loop. A Josephson tunnel junction can for instance be realised with a superconductor-isolator-superconductor (SIS) contact.

The energy resolution of these MMCs is not solely dependent on its intrinsic one but is also influenced by the noise contributions of the SQUIDs used to read them out. With the Josephson junctions being the core of the dc-SQUIDs working principle as well as being an influence on the noise contributions of SQUIDs, it is of particular interest to guarantee a reliable fabrication of high quality JJs. This includes the investigation and optimisation of critical fabrication steps to ensure well-defined tunnel barriers with a homogeneous distribution of the quality parameters on wafer-scale.

As such, in the framework of this thesis, we optimised the sputter deposition of the Nb/Al-AlO_x/Nb based tri-layer in our new PreVAC sputtering system and checked their quality by measuring the *IV*- characteristics of the resulting JJs, extracting the quality parameters thereof. We present the method of recording and minimising the stress the deposited films apply to the SiO₂ substrate. The stress can be minimised by adjusting the sputtering parameters [Ima92b, Du07b], like the driving power of the magnetron sputter gun as well as the pressure of the Ar process gas. For this we adjusted the parameters such that the subsequently deposited thin Al layer completely covers the surface of the bottom Nb electrode in order to have a distinct tunnel barrier shape with low impurity concentration and be homogeneous across the wafer. Furthermore, we continued to focus on a new cross-type junction geometry. The fabrication of so-called cross-type junctions brings along many advantages compared to the more commonly used window-type structures and are discussed in detail in [Bau22].

In chapter 2 we present the necessary theoretical background in order to understand the physics behind Josephson junctions and dc-SQUIDs. It contains a small introduction into the general properties of superconductors. Once that is established, we are able to then derive the physics of the Josephson effects of a Josephson junction and look into the additional effects of applying a magnetic field. We introduce a model with which we can qualitatively describe the *IV*- characteristics of a JJ and even quantitatively in some limiting cases. We then proceed to showcase the different quality parameters one can extract from the *IV*- characteristics of a JJ in order to judge the quality of the JJs produced within this thesis. The chapter ends with the introduction of the working principle of the dc-SQUID and the measuring principle of the JJ capacitance using an unshunted dc-SQUID.

In chapter 3 we showcase the experimental methods used, as well as some results of the optimisation steps. It starts off with the introduction of two different fabrication methods of two different JJ geometries, the so-called cross-type and so-called window-type JJs. We further motivate the change into making the cross-type JJs the new standard for this research group. Subsequently, we present the method of calculating the stress the Nb films apply on the underlying SiO_2 substrate by measuring the curvature of the substrate before and after deposition. We present how the stress affects the surface of the film and what surface property is favourable for a higher quality of the JJs. The results of this optimisation step is shown within this chapter. Additionally, the method to oxidise the Al layer is presented and how the thickness and oxidation parameters affect the critical current density of the finished tri-layer. The chapter ends on the introduction of the four-wire sensing method to characterise the JJs by measuring the *IV*- characteristics at $T = 4.2\text{ K}$ and how one corrects the data due to the finite temperature these JJs were measured at.

In chapter 4 we present the results for the measured cross-type JJs. For this, we recorded the *IV*- characteristics of differently sized JJs with designed JJ areas down to $1\text{ }\mu\text{m}^2$ and extracted the quality parameters from it. This chapter presents low quality JJs as well as high quality JJs and looks into the difference in fabrication steps and how this difference in quality might be explained. Utilising these quality parameters, the real JJ area size is determined to see how much it deviates from the designed area. To account for thermal fluctuations, the data gets corrected correspondingly according to the model of Poisson distribution. This model gets fitted onto the measured data to see how well this thermal fluctuation is described by it. The quality parameters are checked on how well they scale with the JJ area in accordance to the expected scaling. Furthermore, comparisons to the theoretically expected values of some of the quality parameters are investigated. This chapter ends with the results of estimating the JJ capacitance by utilising unshunted dc-SQUIDs and discusses the validity of it.

2. Theoretical Background

In this chapter we are going to introduce the theoretical framework to understand the optimization processes performed in this thesis. We are going to introduce the theoretical foundation and physical models to describe dc-SQUIDs. At first, we look at some basic properties of superconductors, followed up by the workings of a superconductor-isolator-superconductor contact (SIS-contact), which are the more commonly used form of a Josephson tunnel junction. Once we have established the framework, we have all the necessary components to build a basic dc-SQUID and are able to derive its behaviour based on the previous introductions.

2.1 Superconductivity

The first recorded discovery of superconductivity was back in 1911 in an experimental setup investigating the resistance of solid mercury at low temperatures by Heike Kamerlingh Onnes [Onn11]. He found that around a temperature of $T = 4.2\text{ K}$ the resistance of mercury jumps to a value of zero. The additional phenomenon of field expulsion of superconducting material was discovered by Walther Meissner and Robert Ochsenfeld in 1933 [Mei33]. These discoveries led to a new research branch of condensed matter physics. It took roughly 20 years to establish a theoretical model, the BCS theory (named after Bardeen, Cooper, Schrieffer) [Bar57b, Bar57a, Coo56, Sch63]. Since then many new kinds of superconductors and varieties of applications have been found. The BCS theory introduced the model of a new kind of composite boson, the Cooper pair, which results from an attractive interaction of two electrons, under exchange of a virtual phonon, below a material-dependent critical temperature, such that a new paired state of two electrons forms with an energy lower than the Fermi energy and represents the carriers of the supercurrent of a superconductor. These Cooper pairs therefore have a mass of twice the electron mass and a charge of twice the electron charge. This pairing causes a gap in the continuous energy spectrum such that one needs a minimum amount of energy to produce excitations resulting in the dissipationless current of superconductors up until the point where this minimum energy is reached. In the following discussion we assume the results of the BCS theory.

We start our theoretical discussion with Lorentz's law in it's quantum form, i.e. it's corresponding Schrödinger equation

$$i\hbar \frac{\partial \Psi}{\partial t} = \frac{1}{2m} \left(\frac{\hbar}{i} \nabla - q\mathbf{A} \right)^2 \Psi + q\phi\Psi \quad (2.1)$$

which is describing a charged particle in an electromagnetic field with the vector potential \mathbf{A} , a scalar field ϕ resulting from gauge invariance, the charge of the particle q , the mass of the particle m and the wavefunction Ψ . Furthermore, we need the continuity equation of quantum mechanics, which represents the conservation of probability and is given by

$$\frac{\partial \rho}{\partial t} + \nabla \cdot \mathbf{J}_\rho = 0 \quad (2.2)$$

with the probability current \mathbf{J}_ρ being defined as

$$\mathbf{J}_\rho \equiv \frac{\hbar}{2mi} (\Psi^* \nabla \Psi - \Psi \nabla \Psi^*). \quad (2.3)$$

We note that this is based on the Max Born interpretation of the wavefunction, i.e.

$$\rho(\mathbf{r}, t) = |\Psi(\mathbf{r}, t)|^2 \text{ and} \quad (2.4)$$

$$\int \Psi^*(\mathbf{r}, t) \Psi(\mathbf{r}, t) dV = 1. \quad (2.5)$$

Now that we have introduced the basic quantum mechanical concepts, we can start to talk about superconductors, more specifically, their description by a macroscopic wavefunction. In the model of a macroscopic quantum superconductor, the main assumption is that the ensemble of carriers of the supercurrent, Cooper pairs according to the BCS theory, can be described by a coherent macroscopic wavefunction [Gin50]

$$\psi(\mathbf{r}, t) = \psi_0(\mathbf{r}, t) e^{i\theta(\mathbf{r}, t)} = \sqrt{n_s(\mathbf{r}, t)} e^{i\theta(\mathbf{r}, t)}. \quad (2.6)$$

Here, n_s is the number density of Cooper pairs and $\theta(\mathbf{r}, t)$ the macroscopic phase dependent on the position \mathbf{r} of the ensemble and time t . With this hypothesis we are able to explain phenomena of superconductors, such as flux quantization and the Josephson effect. This macroscopic wavefunction can be used as the order parameter to describe the phase transition and is also motivated by the comparatively large coherence length of Cooper pairs [Lon50], i.e. the characteristic size of them.

Now, contrary to the usual definition of the absolute square of the wavefunction being the probability density, we instead define it as Cooper pair density n_s . With that, the volume integral of the absolute squared wave function then becomes the number of Cooper pair particles N_s . This redefinition leads to the probability current density being a current density of superconducting particles, which follows from Equation 2.3 by multiplying it with the charge of the Cooper pair $q_s = -2e$ and inserting Equation 2.6, the current density then yields

$$\mathbf{J}_s = -2en_s(\mathbf{r}, t) \left\{ \frac{\hbar}{m_s} \nabla \theta(\mathbf{r}, t) + \frac{2e}{m_s} \mathbf{A}(\mathbf{r}, t) \right\}. \quad (2.7)$$

Using this expression for the supercurrent density, one can derive the London equations. The second London equation results from taking the curl of Equation 2.7. As the curl of a gradient field, $\nabla \times \nabla \varphi$, is zero, we find

$$\nabla \times \left(\frac{m_s}{4n_s e^2} \mathbf{J}_s \right) = -\mathbf{B}. \quad (2.8)$$

In combination with Ampère's circuital law, this explains the Meißner-Ochsenfeld effect, which shows an exponential decay of an applied magnetic field inside the superconductor with a characteristic penetration length, also known as London penetration depth

$$\lambda_L = \sqrt{\frac{m_s}{4\mu_0 n_s e^2}}. \quad (2.9)$$

The first London equation is derived by taking the partial time derivative of Equation 2.6:

$$\frac{\partial}{\partial t} \left(\frac{m_s}{4n_s e^2} \mathbf{J}_s \right) = \mathbf{E} + \frac{1}{2en_s} \nabla \left(\frac{m_s}{8n_s e^2} \mathbf{J}_s^2 \right). \quad (2.10)$$

The second term on the right-hand side is usually neglected [Buc04], due to its very small contribution, which leaves us with

$$\frac{\partial}{\partial t} \left(\frac{m_s}{4n_s e^2} \mathbf{J}_s \right) = \mathbf{E}. \quad (2.11)$$

This means that for a time-independent supercurrent, the electric field inside the superconductor vanishes, i.e. we have a dissipationless current.

2.1.1 Quantization of Flux

With the previous expressions, we now have the ingredients to see why the magnetic flux through a superconducting ring is quantized. Assuming a homogeneous and isotropic superconductor, one can integrate Equation 2.7 along a closed contour $\partial\Gamma$ while utilising Stoke's theorem to get

$$\oint_{\partial\Gamma} \left(\frac{m_s}{4n_s e^2} \mathbf{J}_s \right) d\mathbf{l} + \int_S \mathbf{B} d\mathbf{s} = -\frac{\hbar}{2e} \oint_{\partial\Gamma} \nabla \theta d\mathbf{l} = -\frac{\hbar}{2e} 2\pi n \quad (2.12)$$

with $n \in \mathbb{Z}$. The last equal sign stems from the fact that, although our wavefunction is uniquely defined, its phase value is only uniquely defined in an interval of 2π . Additionally, if one takes a contour path such that it is in a multiply connected region with a superconducting and a non-superconducting area, e.g. a superconducting ring as seen in Figure 2.1 and takes the path deep inside the superconductor such that the current vanishes, we end up with

$$\int_{\partial\Gamma} \mathbf{B} d\mathbf{s} = n \frac{\hbar}{2e} = n\Phi_0. \quad (2.13)$$

Without loss of generality, we replaced n with $-n$ and introduced the flux quantum $\Phi_0 = 2.067833848\dots \times 10^{-15} \text{Wb}$ [Tie21], which is defined by the fundamental physical constants \hbar and e .

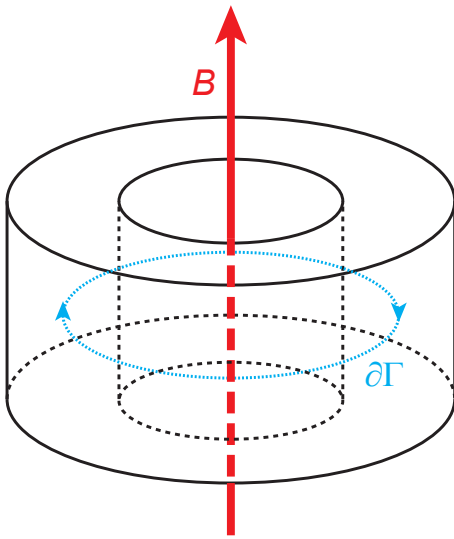


Figure 2.1: Schematic of a superconducting ring with a trapped magnetic field \mathbf{B} inside of it. The dashed blue line $\partial\Gamma$ shows the chosen integration path deep inside the superconducting bulk. The red lines depict the trapped magnetic field lines whose flux through the superconducting ring is quantized.

2.2 Josephson Junction

The weak coupling of two superconducting electrodes is what we know as Josephson junction. The technical realization of this can be and has been done in various ways, such as point contacts or by introducing a thin isolating barrier between the electrodes as has been done within the framework of this thesis. In order to see how a Josephson junction behaves, we first take a look at the Josephson effect.

2.2.1 Josephson Effect

The Josephson effect, named after Brian D. Josephson, who developed this model in 1962 [Jos62] describes the coherent tunneling of Cooper pairs through a potential barrier inbetween two superconductors. The governing equations, the Josephson equations, can be derived by looking at the two superconductors as two separate quantum systems which are symmetrically weakly coupled due to the potential barrier inbetween [Fey64]. The corresponding scheme is depicted in Figure 2.2. The time dependent Schrödinger equations, describing the time development of the wavefunctions of the two superconductors, can be approximated by

$$\dot{\psi}_1 = -\frac{1}{\hbar} [\mu_1 \psi_1 + \kappa \psi_2] \text{ and} \quad (2.14)$$

$$\dot{\psi}_2 = -\frac{1}{\hbar} [\mu_2 \psi_2 + \kappa \psi_1], \quad (2.15)$$

where ψ_i is the wavefunction of superconductor i , μ_i the chemical potential of superconductor i with $i = 1, 2$ and κ the coupling constant, which is mainly determined

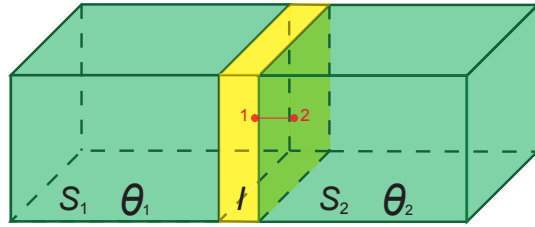


Figure 2.2: Schematic of a superconductor-insulator-superconductor (S_1IS_2) contact. The labels θ_1 and θ_2 indicate the phase of the macroscopic wavefunction of superconductor 1 and superconductor 2. The red line indicates the integration path used to calculate junction specific quantities.

by the overlap of the two wavefunctions. Utilising the macroscopic nature of superconductors in Equation 2.6 and separating real and imaginary part, we find

$$\dot{n}_{s,1} = \frac{2\kappa}{\hbar} n_s \sin(\theta_2 - \theta_1) = -\dot{n}_{s,2} \quad (2.16)$$

$$\text{and } \frac{\partial}{\partial t}(\theta_2 - \theta_1) = \frac{1}{\hbar}(\mu_1 - \mu_2), \quad (2.17)$$

where we used that due to current conservation $\dot{n}_{s,1} = -\dot{n}_{s,2}$ and where we assumed identical superconductors $n_{s,1} = n_{s,2} = n_s$. Equation 2.17 is known as second Josephson equation. Multiplying Equation 2.16 with the volume of superconductor 1 and the charge of the Cooper pairs $q_s = -2e$ results in the first Josephson equation describing the supercurrent

$$I_s = I_c \sin(\varphi) \quad (2.18)$$

with $I_c = \frac{4\kappa e}{\hbar} V n_s$ and φ the gauge-invariant phase difference across the JJ.

The difference in chemical potential can be expressed by

$$\mu_1 - \mu_2 = -2e \int_1^2 \mathbf{E}(\mathbf{r}, t) d\mathbf{l} \quad (2.19)$$

if there is an electric field inside the junction, caused by a voltage applied across the junction. The integration path is shown in Figure 2.2. The gauge-invariant phase difference φ is in general given by [Buc04]

$$\varphi = \theta_2 - \theta_1 - \frac{2\pi}{\Phi_0} \int_1^2 \mathbf{A} d\mathbf{l} \quad (2.20)$$

with \mathbf{A} describing the magnetic vector potential. The additional integral term originates from the integration of the gauge-invariant phase gradient $\gamma = \nabla\theta - \frac{2\pi}{\Phi_0} \mathbf{A}$, which

arises from the gauge invariance of the super current density, turning Equation 2.7 into $J_s(\mathbf{r}, t) = \frac{q_s n_s \hbar}{m_s} \gamma(\mathbf{r}, t)$.

There are now two basic regimes of the Josephson effect. First, the dc-Josephson effect, which is in the regime of constant φ , coming along with zero voltage drop across the junction and the supercurrent being constant in time. This phenomenon is also known as zero-voltage state. In contrary, if we have a constant voltage drop V across the junction, the junction is in the so-called voltage-state, where the ac-Josephson effect occurs. The gauge-invariant phase difference is now time dependent and according to Equation 2.17 given by

$$\varphi(t) = \varphi_0 + \frac{2\pi}{\Phi_0} V t \quad (2.21)$$

and the supercurrent is oscillating with the Josephson frequency $\omega_J = \frac{2\pi}{\Phi_0} V$.

2.2.2 Short Josephson Junctions

Up until now, the mentioned formulae are only viable for point contacts, i.e. zero-dimensional Josephson junctions. In reality, junctions have a certain three-dimensional geometry, as seen in Figure 2.3, that needs to be considered. The junctions produced within the scope of this thesis are classified as short Josephson junctions. This means that the generated magnetic field of the supercurrent, the self-field, is negligible compared to the external applied magnetic field. This is not the case for long Josephson junctions. The quantity that classifies whether a junction is considered short or long is the Josephson penetration depth [Wei69]

$$\lambda_J = \sqrt{\frac{\Phi_0}{2\pi\mu_0 J_c t_B}} \quad (2.22)$$

where $J_c = \frac{I_c}{WL}$ is the critical current density and $t_B = d + \lambda_{L,1} + \lambda_{L,2}$ the magnetic thickness of the junction. W describes the width (parallel to applied magnetic field), L the length and d the thickness of the junction region. If $L \ll \lambda_J$, we have a short junction and a long junction for $L \gg \lambda_J$.

Short Josephson Junction in a Magnetic Field

Applying a magnetic field \mathbf{B} across the junction, such that the vector points parallel to the W edge, as seen in Figure 2.3, leads to a spatial interference effect. This can be seen by taking a path integral, such as the path Γ in Figure 2.3, over the gradient of the phase of the superconductor wavefunction and utilising Equation 2.7 as well

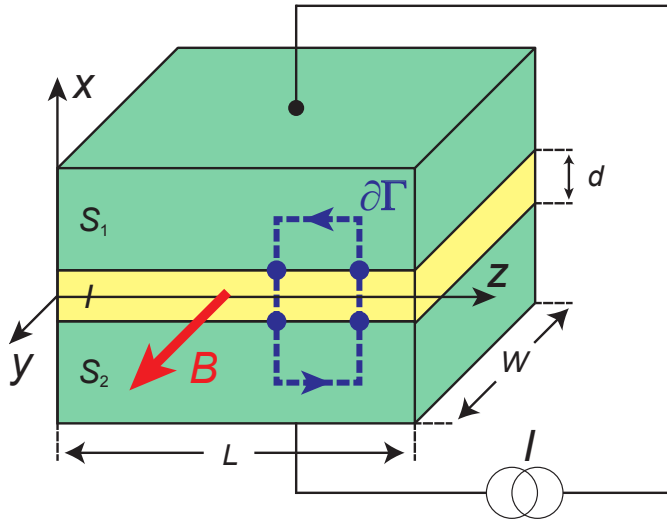


Figure 2.3: Sketch of a short Josephson junction. The area of the tunnel barrier lies in the $y - z$ plane with the current running in x direction and an applied magnetic flux density \mathbf{B} in y -direction.

as Equation 2.20 to find an expression for the total flux enclosed by a contour line around the junction side area [Jos65]:

$$\nabla \varphi(\mathbf{r}, t) = \frac{2\pi}{\Phi_0} t_B \{ \mathbf{B}(\mathbf{r}, t) \times \hat{\mathbf{x}} \} \quad (2.23)$$

For this specific case we find for the supercurrent density

$$\mathbf{J}_s(y, z, t) = \mathbf{J}_c(y, z) \sin \left(\frac{2\pi}{\Phi_0} t_B B_y z + \varphi_0 \right). \quad (2.24)$$

To calculate the supercurrent we now have to integrate over the junction area:

$$I_s(B_y) = \int_{-L/2}^{L/2} \int_{-W/2}^{W/2} J_c(y, z) \sin \left(\frac{2\pi}{\Phi_0} t_B B_y z + \varphi_0 \right) dy dz \quad (2.25)$$

$$= \Im \left[e^{i\varphi_0} \int_{-\infty}^{\infty} i_c(z) e^{ikz} dz \right] \quad (2.26)$$

where $k = \frac{2\pi}{\Phi_0} t_B B_y$, $i_c(z) = \int_{-W/2}^{W/2} J_c dy$. Since $i_c(z) = 0$ for $|z| > L/2$, the integral limits have been changed to plus and minus infinite. From this it follows that the maximum supercurrent is given by the absolute value of the Fourier transform of $i_c(z)$. This expression reminds of the relation that is found in optics for the diffraction pattern of a single slit with width L and a transmission function $i_c(z)$. Assuming that

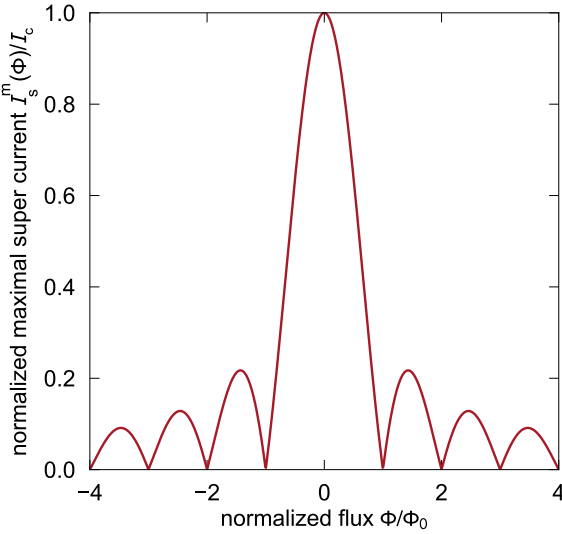


Figure 2.4: Normalized maximal supercurrent plotted against the normalized flux. It vanishes at integer flux quanta and shows local maxima for half-integer flux quanta.

this transmission function is spatially constant, this yields the equation that describes the Fraunhofer diffraction pattern:

$$I_s^m(\Phi) = I_c \left| \frac{\sin \frac{\pi \Phi}{\Phi_0}}{\frac{\pi \Phi}{\Phi_0}} \right| \quad (2.27)$$

with $\Phi = B_y t_B L$ the flux through the junction. The corresponding plot in Figure 2.4 showcases how the maximal supercurrent modulates with the magnetic flux through the barrier and how it can become a method for determining the transmission function, i.e. the current distribution, which has already been done previously in our group [Jak21]. Applying two magnetic fields perpendicular to each other, one can even map out the two-dimensional distribution of the current inside a Josephson junction.

2.2.3 RCSJ Model

Looking at the Josephson junction in the Resistively and Capacitively Shunted Junction (RCSJ) model [McC68], one finds that the Josephson junction does not only consist of a supercurrent channel but also of a resistive and capacitive channel, as schematically drawn in Figure 2.5. At $T = 0$ K, the quasi-particle density is zero since Cooper pairs cannot be broken by thermal excitations. Nonetheless, one finds an ohmic behaviour once the current exceeds I_c due to the Cooper pairs not being able to carry the current anymore. This causes the voltage to jump to the gap voltage, i.e. Cooper pairs break up into quasi-particles, and increases linearly when the current is increased further. Explicitly, the kinetic energy of the Cooper Pairs increases such that the free energy of the normal conducting state becomes more favourable. At finite temperatures, one finds a finite quasi-particle density, which contributes to the

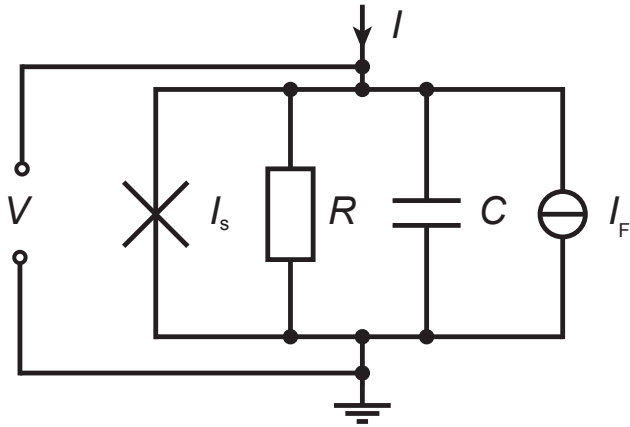


Figure 2.5: Effective circuit of a Josephson junction, as assumed in the RCSJ model. The total current I through the junction is divided into a capacitive current I_D , resistive (or normal) current I_n , superconducting current I_s and fluctuating current I_F .

normal current channel I_n once we have a temporal variation of the phase and thus a voltage drop according to Equation 2.17. Another current channel that we need to consider is the capacitive channel. The SIS-contact can be approximately seen as a parallel plate capacitor with a capacitance $C = \varepsilon_0 \varepsilon_r \frac{A}{d}$ resulting in a displacement current $I_D = \dot{Q} = C \cdot \dot{U}$ if the junction voltage changes with time. The last channel of interest is the fluctuation current I_F . This current consists of different kinds of contributions, such as thermal noise, also known as Nyquist noise [Nyq28, Joh28] with a power spectral density of

$$S_I(f) = \frac{4k_B T}{R_n}, \quad (2.28)$$

and a $1/f$ -noise which becomes dominant at low frequencies and is still a subject of research.

It is important to mention that in the RCSJ model, we assume the normal conductance $G_n = \frac{1}{R_n}$ to be constant in temperature and voltage and we neglect any fluctuation current. A more accurate description for $T = 0\text{ K}$ is

$$G_n(V) = \begin{cases} 0, & \text{for } |V| < 2\Delta/e \\ \frac{1}{R_n}, & \text{for } |V| \geq 2\Delta/e \end{cases} \quad (2.29)$$

with 2Δ being the energy gap to break up Cooper pairs under the assumption that we have identical superconductors. In general the characteristic gap voltage V_{gap} is temperature dependent and given by $V_{\text{gap}} = \frac{\Delta_1(T) + \Delta_2(T)}{e}$. For finite temperatures, we

have a finite number of thermally excited quasi-particles that are able to tunnel at voltages lower than V_{gap} resulting in a finite resistance in this regime:

$$G_n(V, T) = \begin{cases} \frac{1}{R_{\text{sg}}(T)}, & \text{for } |V| < 2\Delta(T)/e \\ \frac{1}{R_n}, & \text{for } |V| \geq 2\Delta(T)/e \end{cases} \quad (2.30)$$

with $\frac{1}{R_{\text{sg}}(T)} = \frac{n(T)}{n_{\text{tot}}} \frac{1}{R_n}$, the sub-gap resistance $R_{\text{sg}}(T)$ and the amount of thermally excited quasi-particles $n(T)/n_{\text{tot}}$. The appearance of a finite resistance at a certain gap voltage is displayed in Figure 2.7. An important characteristic quantity for a Josephson junction is the characteristic voltage

$$V_c = I_c R_n. \quad (2.31)$$

A substitute circuit for a Josephson junction based on a SIS tunnel barrier is shown in Figure 2.5. Using Kirchhoff's Law, Equation 2.18 and Equation 2.17, we can write down the equation for the total current in the system:

$$I = I_s + I_n + I_D + I_F \quad (2.32)$$

$$= I_c \sin(\varphi) + \frac{1}{R} \frac{\Phi_0}{2\pi} \frac{d\varphi}{dt} + C \frac{\Phi_0}{2\pi} \frac{d^2\varphi}{dt^2} + I_F \quad (2.33)$$

For the following discussion we neglect the channel of fluctuating current. Equation 2.32 can then be rewritten as [Cla04]

$$\left(\frac{\hbar}{2e}\right)^2 C \ddot{\varphi} + \left(\frac{\hbar}{2e}\right)^2 \frac{1}{R} \dot{\varphi} + \frac{\partial U_J}{\partial \varphi} = 0, \quad (2.34)$$

introducing a potential $U_J = U_{J0} [1 - \cos(\varphi) - i\varphi]$, which is a function of the phase difference φ and has the shape of a tilted washboard. U_{J0} represents the Josephson

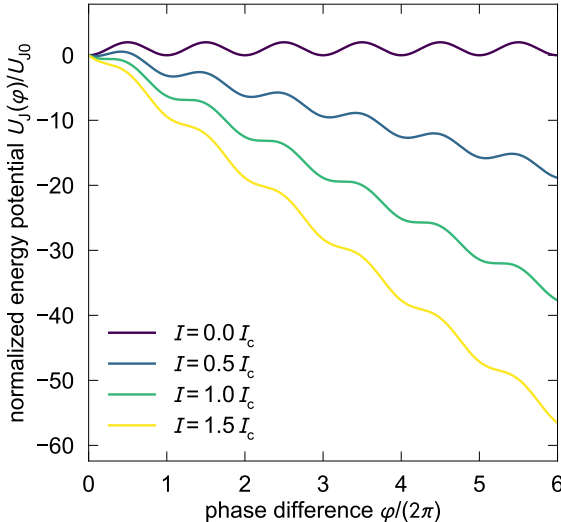


Figure 2.6: The normalized energy potential is plotted against the phase difference for different values of the normalized current. At $i = 1$ the local minima turn into saddle points and at $i > 1$ there are no saddle points or minima left.

coupling energy and $i = I/I_c$ the normalized total current [Jos65]. Equation 2.34 can be interpreted to describe the motion of a phase particle in a tilted washboard potential, as shown in Figure 2.6, with mass $m_\varphi = \left(\frac{\hbar}{2e}\right)^2 C$ and damping $\eta = \left(\frac{\hbar}{2e}\right)^2 \frac{1}{R}$. The tilt of the washboard is proportional to the reduced current i .

By introducing the Stewart-McCumber parameter $\beta_C = \frac{2e}{\hbar} I_c R_n^2 C$ and the normalized time $\tau = \frac{t}{\tau_c} = \frac{t}{2eI_cR/\hbar}$ we get the dynamic equation of a single Josephson junction in reduced units:

$$\beta_C \frac{d^2\varphi}{d\tau^2} + \frac{d\varphi}{d\tau} + \sin(\varphi) - i - i_F(\tau) = 0 \quad (2.35)$$

With the analogy of a phase particle rolling down a tilted washboard potential one can derive the qualitative behaviour of the current-voltage characteristic (*IV*-characteristics) of a Josephson junction. There are generally two cases, the overdamped case with η being large and/or m_φ being small and the underdamped case with η being small and/or m_φ being large, see Figure 2.7. These two cases can be more simply expressed in terms of the Stewart-McCumber parameter β_C with underdamped corresponding to $\beta_C \gg 1$ and overdamped corresponding to $\beta_C \ll 1$. For both cases, the behaviour of increasing the current from zero to I_c is identical. Imagining a particle inside one of the potential minima, the particle will not move until we tilt the washboard potential such that the minima disappear and the particle is able to roll down. This is what happens once the critical current is reached, and the phase starts to change with time, i.e. we measure a voltage drop, see Equation 2.17. Once we exceed the critical current, the voltage increases rapidly at first and then changes over to a linear ohmic behaviour when the current is increased further.

The difference between those cases, lies in what happens if we decrease the current starting from the ohmic behaviour regime. Tilting the washboard potential back until minima start to appear again, equivalent to going below the critical current, the motion of the phase particle will stop immediately for the overdamped case, thus leading back to the zero-voltage-state and therefore to dissipationless current. In the underdamped case on the other hand, the particle has still enough kinetic energy to hop over the potential barriers that appear below I_c . We therefore have still a voltage drop up to a point where the barriers become too high for the particle to overcome. This happens at a recapture current I_r which can be calculated by [Lik86]

$$I_r = \frac{4}{\pi\sqrt{\beta_C}} I_c. \quad (2.36)$$

In total, we expect a hysteretic behaviour for the underdamped case but not for the overdamped case. Another thing to note is that once the phase particle is trapped in one of the minima of the potential for $i < 1$, it is oscillating with a frequency of

$$\omega_0 = \omega_p \left(1 - i^2\right)^{1/4} \quad (2.37)$$

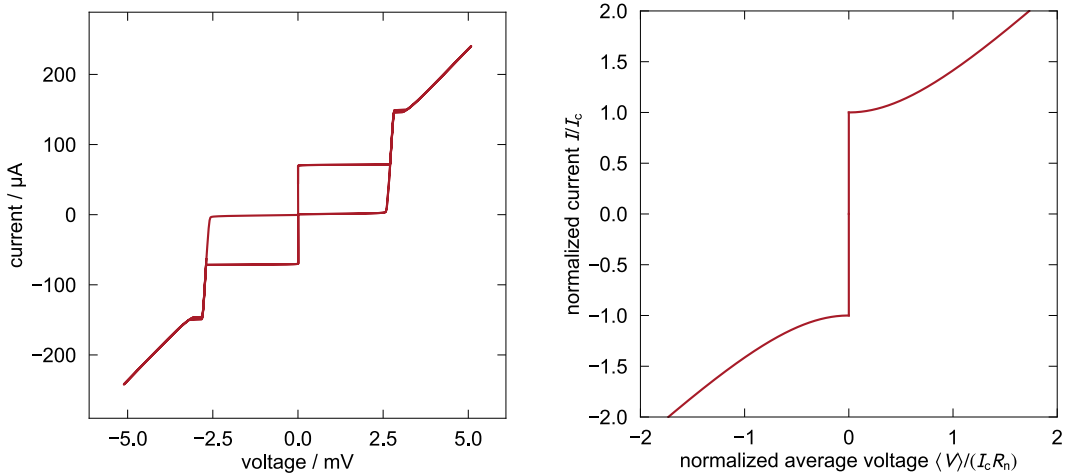


Figure 2.7: Left: Measured IV -characteristics for a cross-type JJ, which has been fabricated in the framework of this thesis and showcases the behaviour which one would expect for an underdamped JJ with $\beta_C \gg 1$. Right: Theoretically expected IV -characteristics for a overdamped JJ in the framework of the RCSJ model under the assumption of a constant resistance and $\beta_C \ll 1$.

with $\omega_p = \sqrt{2\pi I_c/\Phi_0 C}$ being the plasma frequency of the Josephson junction. In this situation, the average velocity $\langle \dot{\phi} \rangle$ and therefore the average voltage is zero.

For strongly overdamped junctions, $\beta_C \ll 1$, in the voltage state, the time averaged voltage drop across the Josephson junction can be derived in the RCSJ model to be

$$\langle V(t) \rangle = I_c R_n \sqrt{\left(\frac{I}{I_c}\right)^2 - 1}, \quad (2.38)$$

as shown on the right of Figure 2.7, which is free of hysteresis. If we now take thermal fluctuations due to finite temperatures $T > 0$ as well as the finite normal state resistance R_n into account, the current at which the particle starts to roll down the potential is reduced. One can model these thermal fluctuations with the concept of Brownian motion [Ful72]. At finite temperature T , the current at which we switch to the voltage state, is then called switching current I_{sw} and is following a Poisson distribution $P(I_{\text{sw}})$ [Cas96]. This distribution is described by the recursive formula

$$P(I_{\text{sw}}) = \tau_{\text{th}}^{-1}(I_{\text{sw}}) \left(\frac{dI}{dt} \right)^{-1} \left(1 - \int_0^{I_{\text{sw}}} P(I) dI \right) \quad (2.39)$$

and represents the probability of the Josephson junction switching into the voltage state at the current I_{sw} in the interval dI when applying a current ramp with the rate dI/dt . τ_{th} describes the lifetime of the voltage state or, in other words, how

long the phase particle stays in a minimum and is depending on the height of the potential

$$U_0 = 2U_{J0} \left(\sqrt{1 - i^2} - i \arccos i \right) \quad (2.40)$$

as well as the oscillation frequency ω_0 and has the following functional form [Kra40]:

$$\tau_{\text{th}}^{-1} = a_{\text{th}} \frac{\omega_0}{2\pi} e^{-U_0/k_B T}. \quad (2.41)$$

The prefactor

$$a_{\text{th}} \approx \frac{4}{\left(\sqrt{1 + Q_J k_B T / 1.8 U_0} + 1 \right)^2} \quad (2.42)$$

contains the quality factor $Q_J = \omega_0 R_{nC}$ of the Josephson junction and is rather small for the hysteretic junctions produced within the scope of this thesis such that we are able to approximate $a_{\text{th}} \approx 1$ [Bue83, Sil88]. Since the conducted measurements were done at $T = 4.2$ K the dominating mechanism is the thermal activation of the phase particle and we are able to neglect the effect of quantum tunneling [Dev85].

2.3 Quality Criteria for Josephson Junctions

To decide whether a Josephson junction is of good quality, the current-voltage characteristic needs to be checked. How much information is extractable out of the *IV*-characteristics, depends entirely on the Stewart-McCumber parameter β_C . In general, one might want to completely avoid hysteresis, nonetheless, not only is hysteresis unavoidable when optimizing the energy resolution, which leads to $\beta_C \approx 1$, see subsection 2.4.3, but it also leads to more quality parameters that can be extracted from the *IV*-characteristics. This slightly underdamped case was already qualitatively discussed in subsection 2.2.3 in the RCSJ-model. In practical applications, the resistance is in fact voltage and temperature dependent, such that the assumption of the RCSJ-model is not working anymore but is still a valid model for a qualitative discussion of the hysteretic behaviour. Figure 2.8 shows an example of a *IV*-characteristics of an underdamped junction. Parameters that can be extracted, are the critical current I_c or switching current I_{sw} , the retrapping current I_r , the gap current I_{gap} , the gap voltage $V_{\text{gap}} = 2\Delta(T)/e$, the subgap resistance R_{sg} and the normal resistance R_n . The gap current is a quantity which is used for data correction as we will see later in subsection 3.3.2. The subgap resistance can be measured in the regime below the gap voltage and occurs due to thermal excitation of Cooper pairs that leads to a finite amount of quasi-particles. Other mechanisms that lead to a quasi-particle conduction are multi-photon processes or pinholes in the tunneling barrier. Above the gap voltage, when enough energy by the current source is supplied to break up the Cooper pairs, we have the ohmic regime where we observe the normal state resistance.

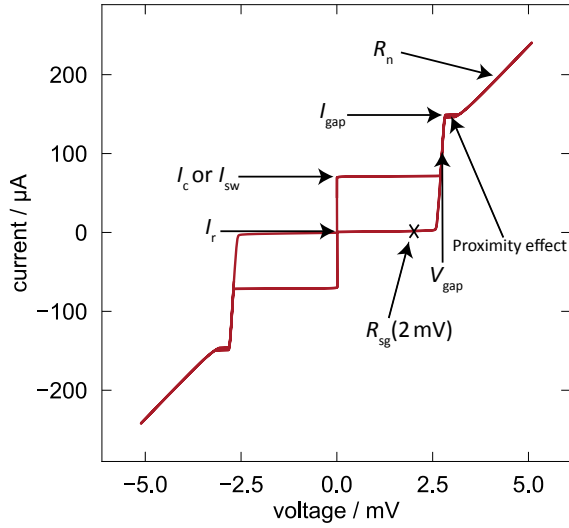


Figure 2.8: Hysteretic IV-characteristics of an underdamped cross-type JJ fabricated and measured within the framework of this thesis. Various quality parameters that can be extracted from the IV-curve are denoted here.

2.3.1 Gap Voltage V_{gap}

The gap voltage V_{gap} is one of the important properties of the superconducting material used for the junction. According to the BCS theory in the weak coupling limit, we can calculate the gap energy at vanishing temperatures to be $\Delta_0 = 1.764 k_B T_c$ [Buc04]. Unfortunately, this relationship does not hold for type-2 superconductors like niobium and has to be replaced by empirically determined values [Car90] with $\frac{\Delta_0}{k_B T_c}$ in between 1.92 and 1.97 and Δ_0 between 1.53 meV and 1.57 meV. For the temperature dependence of the gap energy Δ , approximations have been found [Buc04] in the weak-coupling regime, which we do not have in the case of niobium but is a good approximation nonetheless [Buc04] and for $T < 0.5T_c$ the dependence is given by

$$\frac{\Delta(T)}{\Delta_0} \approx 1 - 3.33 \left(\frac{T}{T_c} \right)^{1/2} \exp \left(-1.76 \cdot \frac{T_c}{T} \right). \quad (2.43)$$

For a full description over the whole temperature range, the BCS theory [Bar57b, Bar57a] provides the formula

$$\frac{2}{\tilde{V}_0 D(E_F)} = \int_0^{\hbar \omega_D} \frac{d\varepsilon}{\sqrt{\varepsilon^2 + \Delta^2(T)}} \tanh \left(\frac{\sqrt{\varepsilon^2 + \Delta^2(T)}}{2k_B T} \right) \quad (2.44)$$

to calculate the temperature dependence of the energy gap Δ but is only numerically solvable. Here, ω_D is the Debye frequency, $\tilde{V}_0 D(E_F)$ the interaction potential of the Cooper pairs on the Fermi surface. Since the temperature regime that has been investigated in the context of this thesis lies around 4.2 K, the description in Equation 2.43 is a good theoretical approximation. Taking the literature values for

the superconducting energy gap of niobium and the critical temperature $T_c \approx 9.25$ K, the theoretical gap voltage is in the range of

$$V_{\text{gap, theo}} = 2.83 \text{ mV} \dots 2.93 \text{ mV}. \quad (2.45)$$

Deviations from this optimal theoretical values are caused by films of the superconducting electrodes being thinner than the magnetic penetration depth λ or having a lower critical temperature than bulk niobium. Closely related to good superconducting properties is the film stress of the deposited superconducting material. For optimal properties, one strives for a completely stress free or slightly compressive film [Ima92b, Ima92a, Du07b].

2.3.2 $I_c R_n$ Product

As we have seen in subsection 2.2.1, one of the material dependent quantities of the Josephson effect is the critical current density. The critical supercurrent density through a potential barrier is given by

$$J_c = \frac{e\hbar\sqrt{n_{s,1}n_{s,2}}}{m_e\kappa \sinh(d/\kappa)} \quad (2.46)$$

with $\kappa = \sqrt{\frac{\hbar^2}{2m_e(V_0 - \varepsilon_0)}}$ being a tunneling barrier specific quantity, d the barrier thickness, ε_0 the kinetic energy of the Cooper pairs and V_0 the height of the potential barrier. This relation can be determined by solving the stationary Schrödinger equation with the corresponding boundary conditions of the potential barrier [Lan80]. Integrating this density over the junction area yields the critical current, which is dependent of the barrier thickness. The critical current I_c decreases with increasing barrier thickness d . On the other hand, we have the normal resistance R_n which is also dependent on the junction geometry and will increase with increasing d . As such, one is inclined to believe that the $I_c R_n$ product is a geometry independent quantity of a Josephson contact. This has been analytically shown in the Ambegaokar-Baratoff-theory [Amb63], which suggests for a SIS contact the relationship [Lik86]

$$I_c R_n = \frac{\pi}{2e} \Delta(T) \tanh \left[\frac{\Delta(T)}{2k_B T} \right]. \quad (2.47)$$

Note that this formula was derived for a perfectly shaped rectangular potential describing the tunneling barrier, which never occurs in real world applications. Since the $I_c R_n$ product describes the ideal Cooper pair tunneling, it can be used as a quality parameter as long as no excess current is present. The excess current I_{exc} presents itself in the IV -characteristics as an intersection point of the current axis and the straight line of the ohmic dependent regime. If this value is above zero, quasi-particle

conduction is contributing to the critical current, thus voiding the $I_c R_n$ product as a measure of Cooper pair tunneling.

In order to achieve ideal tunneling in real Josephson junctions based on Nb/Al-AlO_x/Nb tri-layers, they must have a distinct AlO_x barrier with homogeneous thickness and without any impurities.

2.3.3 Subgap Resistance R_{sg}

Since the temperature at which the JJs were measured was at $T = 4.2\text{ K}$, the Cooper pair density is slightly decreased. The temperature dependence of the Cooper pair density is according to the Gorter-Casimir two-fluid model [Gor34] given by

$$n_s(T) = n_s(0) \left[1 - \left(\frac{T}{T_c} \right)^4 \right]. \quad (2.48)$$

This results in a more than 4 % share of broken Cooper pairs, which contribute to a subgap conductance of quasi-particles and cannot be avoided regardless of how high the quality of the JJ itself is.

For the subgap branch we find the characteristic subgap resistance R_{sg} , which, in contrast to the normal resistance, is voltage dependent. This means that one needs to define a voltage point across all junctions where this quantity is measured in order to have a direct comparison. The subgap resistance is furthermore a measure of how much leakage current is present in a given JJ and one wants in general to have a very high $R_{sg}(V)$. For Nb/Al-AlO_x/Nb tri-layers, it is common that the subgap resistance gets evaluated at a voltage of 2 mV. This rather high voltage point was chosen since the SQUID is usually operated in the voltage state. Once the subgap resistance is determined from the IV -characteristics, one can calculate the resistance ratio R_{sg}/R_n , which is independent of the geometry of the junction, making it a good comparison value for different junctions of the same material and fabrication process. Here as well, a high value of the ratio, thus a low leakage current, indicates a high quality.

2.4 dc-SQUIDs

We have now collected all the parts to build a basic Superconducting Quantum Interference Device (SQUID). A direct current or dc-SQUID contains two Josephson junctions that are connected to each other in parallel forming a superconducting loop, see Figure 2.9. This configuration enables us to measure changes in the magnetic field, e.g. in units of the magnetic flux quantum by utilising the dc-SQUID as a flux-to-voltage transducer.

2.4.1 Zero Voltage State

Feeding a current through this loop, results in the current to split up into the two branches, each containing a JJ. Assuming identical Josephson junctions, the total supercurrent is

$$I_s = I_c [\sin \varphi_1 + \sin \varphi_2] = 2I_c \cos\left(\frac{\varphi_1 - \varphi_2}{2}\right) \sin\left(\frac{\varphi_1 + \varphi_2}{2}\right). \quad (2.49)$$

Here, φ_i represents the phase difference of junction $i = 1, 2$. Similar to the calculation done in subsection 2.1.1 we can find an expression for the gauge-invariant phase differences φ_1 and φ_2 of the two junctions by choosing an integration contour inside the SQUID loop:

$$\varphi_2 - \varphi_1 = \frac{2\pi\Phi}{\Phi_0} \quad (2.50)$$

with the total magnetic flux Φ running through the superconducting loop. Inserting this expression into the previous, one then obtains

$$I_s = 2I_c \cos\left(\pi \frac{\Phi}{\Phi_0}\right) \sin\left(\varphi_1 + \pi \frac{\Phi}{\Phi_0}\right), \quad (2.51)$$

which means that the maximum supercurrent is given by

$$I_s^m = 2I_c \left| \cos\left(\pi \frac{\Phi}{\Phi_0}\right) \right|. \quad (2.52)$$

From this, one can immediately see why SQUIDs are called interference devices. The expression above is the same one finds for the intensity of diffracted light behind a double slit [Jen67]. So instead of electromagnetic waves interfering we have the superconducting wave functions of both arms interfering with each other causing the modulation of the maximum supercurrent. The total flux Φ inside a SQUID is given by

$$\Phi = \Phi_{\text{ext}} + LI_{\text{cir}} \quad (2.53)$$

with the externally applied magnetic flux Φ_{ext} and an intrinsic screening flux $\Phi_L = LI_{\text{cir}}$ caused by the finite inductance of the SQUID loop and the circulating screening current $I_{\text{cir}} = \frac{I_{s1} - I_{s2}}{2}$. The total flux can then be written as

$$\Phi = \Phi_{\text{ext}} - LI_c \sin\left(\pi \frac{\Phi}{\Phi_0}\right) \cos\left(\varphi_1 + \pi \frac{\Phi}{\Phi_0}\right) \quad (2.54)$$

or by introducing the screening parameter $\beta_L = \frac{2LI_c}{\Phi_0}$, be written as

$$\Phi = \Phi_{\text{ext}} - \frac{1}{2} \beta_L \Phi_0 \sin\left(\pi \frac{\Phi}{\Phi_0}\right) \cos\left(\varphi_1 + \pi \frac{\Phi}{\Phi_0}\right). \quad (2.55)$$

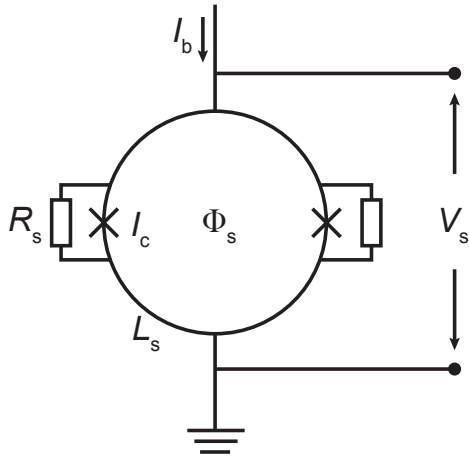


Figure 2.9: Sketch of a dc-SQUID. The Josephson junctions are connected in parallel forming a loop structure with the SQUID inductance L_s . A bias current I_b is pushed through the SQUID and the voltage drop V_s is measured. The JJs are additionally shunted with shunt resistors R_s to avoid a hysteretic behaviour in the IV -characteristics.

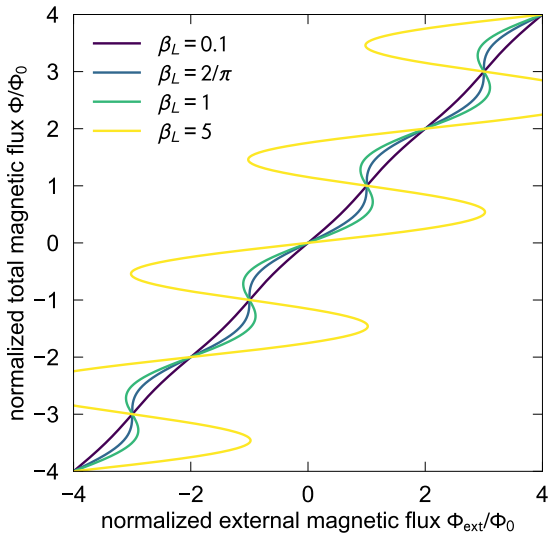


Figure 2.10: Total magnetic flux Φ threading the SQUID loop plotted against the externally applied flux Φ_{ext} for different values of the screening parameter β_L . Hysteretic behaviour appears for $\beta_L > 2/\pi$.

For small supercurrents $I_s \ll 2I_c$, we can derive from Equation 2.51 the relation $\sin(\varphi_1) \approx -\sin(\varphi_2)$. This simplifies Equation 2.55 into

$$\Phi = \Phi_{\text{ext}} - \frac{1}{2}\beta_L\Phi_0 \sin\left(\pi\frac{\Phi}{\Phi_0}\right). \quad (2.56)$$

Figure 2.10 showcases how the total flux Φ changes with the value of the external flux Φ_{ext} , modulated by the flux due to the screening current, for different values of the screening parameter β_L . We note that for $\beta_L > 2/\pi$, the curve turns hysteretic and we may get multiple values of the total flux for the same value of the external flux.

Having this screening parameter introduced, one can look at two limiting cases, analogous to 2.2.3. For negligible screening $\beta_L \ll 1$, one can simply replace the total

flux Φ by the external flux Φ_{ext} . For very large screening $\beta_L \gg 1$, the circulating current combined with the high inductance compensates any applied flux. This means that the SQUID loop can be treated as a closed superconducting loop with the total flux quantized: $\Phi = \Phi_{\text{ext}} + \Phi_L \simeq n\Phi_0$.

2.4.2 Voltage state

If it comes to practical applications of dc-SQUIDs, the voltage state is the *modus operandi*. Here we drive a constant bias current above the maximum supercurrent at zero flux $I_s^m(0)$ through the SQUID such that the normal current channel is contributing. In the following, we showcase how this mode of operation will result in an output voltage which depends on the applied magnetic flux.

Just like in subsection 2.2.3, we treat both junctions in the RCSJ model and simply apply Kirchhoff's law to arrive at the following set of equations [Tes77, Bru82, Waa84]:

$$\frac{I}{2} - I_{\text{cir}} = \frac{\hbar C}{2e} \frac{d^2\varphi_1}{dt^2} + \frac{\hbar}{2eR_n} \frac{d\varphi_1}{dt} + I_c \sin(\varphi_1) + I_{F1} \quad (2.57)$$

$$\frac{I}{2} + I_{\text{cir}} = \frac{\hbar C}{2e} \frac{d^2\varphi_2}{dt^2} + \frac{\hbar}{2eR_n} \frac{d\varphi_2}{dt} + I_c \sin(\varphi_2) + I_{F2} \quad (2.58)$$

$$\varphi_1 - \varphi_2 = 2\pi \left(n + \frac{\Phi_{\text{ext}}}{\Phi_0} + \frac{LI_{\text{cir}}}{\Phi_0} \right) \quad (2.59)$$

Note that we assumed identical junctions, which is a good approximation for the junctions investigated within this thesis. Looking at the limiting case of $\beta_L \ll 1$ and $\beta_C \ll 1$, one finds a similar behaviour to a single Josephson junction for the dependence of the average voltage $\langle V \rangle$ across the SQUID on the bias current I [Cla04], see Equation 2.38:

$$\langle V(t) \rangle = I_c R_n \sqrt{\left(\frac{I}{2I_c} \right)^2 - \left[\cos \left(\pi \frac{\Phi_{\text{ext}}}{\Phi_0} \right) \right]^2} \quad (2.60)$$

But now this voltage also depends on the magnetic flux enclosed by the SQUID. From this expression one can now see why the dc-SQUID is used as flux-to-voltage transducer and that its periodic modulation is in steps of flux quanta, as seen in the periodic IV -characteristics of Figure 2.11. The periodicity of the resulting time-averaged voltage corresponds to a single flux quantum and does not change for different bias currents. The positions of the minima and maxima also do not change for different bias currents. Maximum modulation of the voltage is reached for a bias current of $I \approx 2I_c$ for this particular limiting case.

One can also recognize that the corresponding *IV*-characteristics is similar to a single Josephson junction in the $\beta_C \ll 1$ limit for a constant applied magnetic field. As seen in subsection 2.1.1, for a single Josephson junction we also observed a modulation of the maximum supercurrent by the applied magnetic field which resembled the shape of a Fraunhofer pattern. One of the main reasons of constructing a SQUID lies in increasing the sensitivity by increasing the area the magnetic field threads through.

Nonetheless, the expression above is simply a limiting case example and generally does not apply to dc-SQUIDs used in practice due to the limiting cases not corresponding to the optimal parameters, as we will see in the next subsection.

2.4.3 Optimal Parameters

To discuss the optimisation of dc-SQUIDs, we will shortly discuss how we operate the SQUID and what parameters we need to fine-tune to get the best sensitivity for this flux measurement device. As previously mentioned, the dc-SQUID is usually operated in the voltage state, which means we drive a bias current $I > 2I_c$ through the SQUID or apply a bias voltage V such that we have a periodic voltage signal as a function of magnetic flux. The corresponding current-voltage characteristics as well as the voltage-flux curve can be seen in Figure 2.11. The current at which the

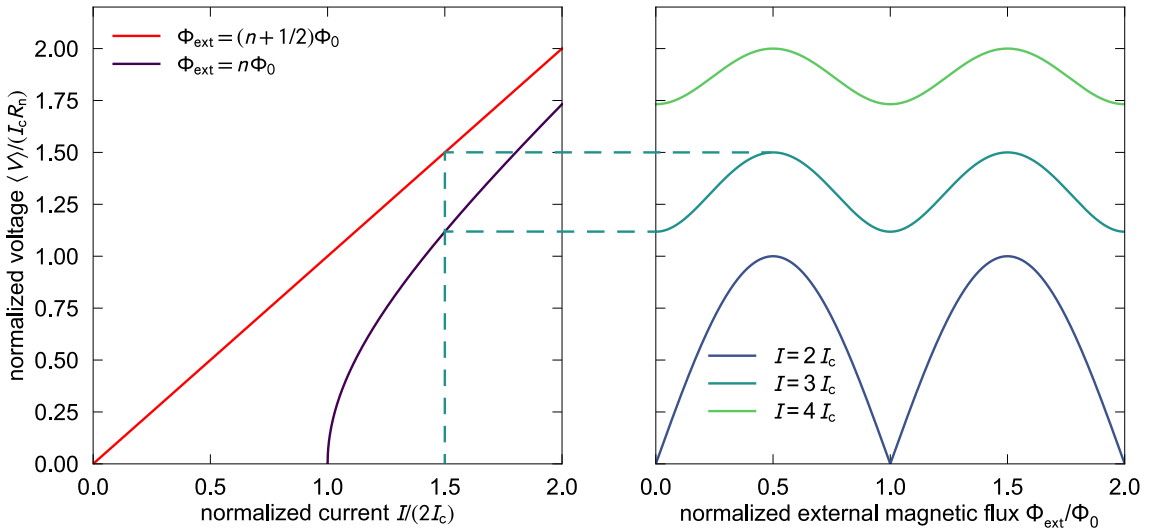


Figure 2.11: Left: *IV*-characteristics of a dc-SQUID in the limiting case of $\beta_L \ll 1$ and $\beta_C \ll 1$. Depending on the external flux Φ_{ext} the critical current varies between $2I_c$ and 0. Right: corresponding voltage-flux characteristics of the dc-SQUID according to the plot on the left.

maximum voltage amplitude is achieved at $I_{\max} = 2I_c$ and the corresponding voltage amplitude $V_{\text{amp}} = I_c R_n$.

Operation

In order to achieve a high resolution, we want the highest possible flux-to-voltage transfer coefficient when operating the SQUID with bias current and the maximum flux-to-current transfer coefficient in voltage bias mode:

$$V_\Phi \equiv \left| \left(\frac{\partial V}{\partial \Phi_{\text{ext}}} \right)_{I=\text{const.}} \right| \quad (2.61)$$

$$I_\Phi \equiv \left| \left(\frac{\partial I}{\partial \Phi_{\text{ext}}} \right)_{V=\text{const.}} \right| \quad (2.62)$$

In the discussed limiting case of $\beta_L \ll 1$ and $\beta_C \ll 1$, the maximum would be achieved at a flux bias of $(2n+1)\Phi_0/4$. For maximum modulation of the voltage curve in bias current mode we choose the bias current to be $I \geq 2I_c$. In order to not deteriorate V_Φ , we need the critical current to be much larger than the thermal current. It has been shown via numerical simulations [Cla88] that the following condition needs to be fulfilled:

$$\frac{1}{5}I_c \geq I_{\text{th}} \equiv \frac{2\pi k_B T}{\Phi_0} \quad (2.63)$$

This is usually fulfilled at 4.2 K in the case of our produced SQUIDs since $I_c \geq 1 \mu\text{A}$.

Noise

For practical applications, where we have to deal with non-zero temperatures, noise becomes prevalent. Based on the Nyquist theorem [Nyg28, Joh28], the resistance of the Josephson junction causes a noise voltage with a power spectral density

$$S_V(f) = 4k_B T R, \quad (2.64)$$

which in turn causes a voltage noise across the dc-SQUID but also a current noise through the SQUID loop. The total noise of a SQUID can be split up into two parts: the $1/f$ -noise scaling inversely with frequency f and the white noise. At high frequencies, the contribution due to the white noise is dominating. In this limit we can split up the spectral density into two contributions. One is given by the thermal voltage fluctuations across the SQUID which depends on the dynamical resistance $R_{\text{dyn}} = \frac{\partial V}{\partial I}$, the other is due to the circulating current, whose path sees a total resistance of $2R_n$. It has been shown that the voltage noise power spectral density is then given by [Lik86, Ryh89, Can91]

$$S_V(f) = V_\Phi^2 \frac{4k_B T L^2}{2R_n} + 4k_B T R_{\text{dyn}}. \quad (2.65)$$

If we look at the limiting case of $\beta_C \ll 1$ and $\beta_L \ll 1$ for which analytical solutions exist, we can further solve the equation above. The maximum voltage swing, which according to Equation 2.60 is given by $\Delta V = V(\Phi_{\text{ext}} = n\Phi_0 + \Phi_0/2) - V(\Phi_{\text{ext}} = n\Phi_0)$, is reached for a bias current $I = 2I_c$ and therefore given by $I_c R_n$. Furthermore, the transfer coefficient V_Φ is largest at magnetic fluxes of $\Phi = \Phi_0(n/2 + 1/4)$. Using the information we provided so far in this limiting case, the dynamic resistance can be calculated to be $R_{\text{dyn}} = R_n/\sqrt{2}$. Fortunately, this value is a good approximation even for higher values of β_L [Cla04]. Nonetheless, numerical simulations [Tes77, Bru82] have shown that the flux-to-voltage transfer coefficient is varying with β_L and given by

$$V_\Phi \approx \frac{2I_c R_n}{\Phi_0(1 + \beta_L)}. \quad (2.66)$$

A characteristic quantity to determine the resolution of a SQUID is the flux noise with a power spectral density of

$$S_\Phi(f) = \frac{S_V(f)}{V_\Phi^2}. \quad (2.67)$$

To compare SQUIDs with different loop inductances, a more appropriate quantity would be the spectral noise energy density

$$\varepsilon(f) = \frac{S_\Phi(f)}{2L} = \frac{S_V(f)}{2LV_\Phi^2}, \quad (2.68)$$

which is also called energy resolution. Plugging our previous results into Equation 2.68, yields [Ryh89, Can96]

$$\varepsilon(f) \approx k_B T \frac{L}{R_n} \left[1 + \frac{\sqrt{2}(1 + \beta_L)^2}{\beta_L^2} \right] = k_B T \frac{\sqrt{\pi LC \beta_L}}{\beta_C} \left[1 + \frac{\sqrt{2}(1 + \beta_L)^2}{\beta_L^2} \right]. \quad (2.69)$$

For optimal performance, one wants to minimize the energy resolution, hence the maximization of V_Φ and L . Nonetheless, one is limited in the SQUID loop inductance L due to increasing thermal noise fluctuations. Numerical computations have shown [Lik86] that

$$L \leq \frac{\Phi_0^2}{20\pi k_B T}, \quad (2.70)$$

which yields an upper limit of roughly 1 nH at $T = 4.2$ K. If one now considers all conditions mentioned so far, the optimized parameters, as found via numerical simulations, are $\beta_C \approx 1 \approx \beta_L$, from which we obtain an energy sensitivity of

$$\varepsilon(f) \simeq 12k_B T \sqrt{LC}. \quad (2.71)$$

We note once more that this equation is based on the assumption that the Josephson junctions are non-hysteretic. But since we have hysteretic junctions with $\beta_C > 0.7$,

we have to include voltage noise of the junctions caused by voltage jumps of hysteretic junction as well as Nyquist-noise caused by high harmonics of the Josephson frequencies [WE96]. For those reasons, a better approximation for the energy sensitivity would be $\varepsilon(f) \simeq 16k_B T \sqrt{LC}$ which was found by numerical simulations in the regime of $\beta_C \approx 1$ and $\beta_L \approx 1$ [Bru82].

One is now inclined to think that we can arbitrarily decrease $\varepsilon(f)$ by decreasing the temperatures for instance. However, there are two things that will give us lower limits for the energy sensitivity. First, we have to consider the hot electron effect, the phenomenon in which the temperature of electrons within the shunt resistors decouple from the phonons of shunt resistors and substrate and won't decrease further than a certain minimum temperature given by design and material properties [Wel94]. The other effect is the quantum limit or Heisenberg's uncertainty principle itself.

In addition to the white noise we discussed so far, we need to bring the $1/f$ -noise into the total spectral density. The flux noise spectral density is then given by

$$S_\Phi = S_{\Phi,w} + \frac{S_{\Phi,1/f}(1 \text{ Hz})}{f^\alpha} \quad (2.72)$$

with $S_{\Phi,w}$ the frequency-independent white noise part and α an empirically determined exponent [Dru11] with values usually between 0.5 and 1, describing the frequency dependence of the $1/f$ -noise, which has a power density at 1 Hz parameterized by $S_{\Phi,1/f}(1 \text{ Hz})$.

Besides the temperature, the inductance as well as the capacitance are quantities that can be minimised to improve the energy sensitivity. These are nonetheless, mostly limited by fabrication technologies.

2.5 Unshunted dc-SQUIDs

In order to adjust the Steward-McCumber parameter β_C reliably for energy resolution or noise optimisation, it is of great importance to know the intrinsic capacitance of the junctions. One way of determining the capacitance of the junctions, or rather the total capacitance of a dc-SQUID, is by measuring the resonant characteristics of an unshunted dc-SQUID. So-called Shapiro steps [Sha63] appear in the corresponding IV -curve, as seen in Figure 4.8. To understand how these steps emerge, we once again utilise the RCSJ model and see what happens if we apply an alternating voltage $V_{ac} = V_{dc} + V_{ac} \cos(\omega_{ac}t)$ across a Josephson junction. Integrating the second Josephson relation then yields

$$\varphi(t) = \varphi_0 + \frac{2\pi}{\Phi_0} V_{dc} t + \frac{2\pi}{\Phi_0} \frac{V_{ac}}{\omega_{ac}} \sin(\omega_{ac}t) \quad (2.73)$$

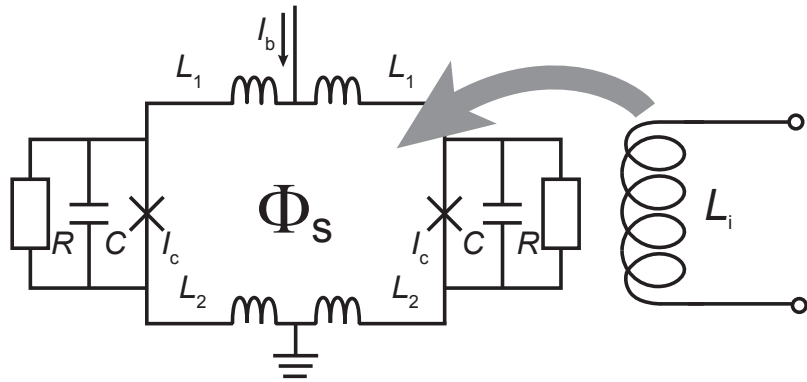


Figure 2.12: Effective circuit of an unshunted dc-SQUID consisting of the total inductance $L_s = 2L_1 + 2L_2$, the two JJs with capacitance C and their intrinsic resistances R . A bias current I_b is applied while a Helmholtz coil with inductance L_i creates a flux through the SQUID loop.

with an integration constant φ_0 . Inserting this into the first Josephson relation we then obtain

$$I_s(t) = I_c \sin \left[\varphi_0 + \frac{2\pi}{\Phi_0} \frac{V_{ac}}{\omega_{ac}} \sin(\omega_{ac}t) \right], \quad (2.74)$$

which can be expressed in a series of Fourier-Bessel functions [Sha64], which yields

$$I_s(t) = \sum_{n=-\infty}^{+\infty} (-1)^n J_n \left(\frac{2\pi V_{ac}}{\Phi_0 \omega_{ac}} \right) \sin[(\omega_{dc} - n\omega_{ac})t + \varphi_0]. \quad (2.75)$$

In this form of expression, one can now see that applying an alternating voltage, the Josephson junction can respond with a dc current once the time dependent argument in the sine function vanishes. This condition is expressed as $\omega_{dc} = n\omega_{ac}$ or $V_{dc} = V_n = n \frac{\Phi_0}{2\pi} \omega_{ac}$. Under fulfilment of this condition, current steps become visible in the IV -characteristics [Coo65].

These current or Shapiro steps not only become visible in Josephson junctions but also in unshunted dc-SQUIDs. In the schematic circuit, seen in Figure 2.12, one can see that the unshunted dc-SQUID can be depicted within the scope of the RCSJ-model with the addition of considering the finite inductance of the SQUID loop. Due to the missing shunts, the Josephson junctions will behave hysteretically and the SQUID loop can be effectively described by an $L_s C_s$ circuit with $L_s = 2L_1 + 2L_2$ and $C_s = C/2$. In the voltage state of the SQUID with constant voltage V_s we have an ac Josephson current with frequency $\omega_J = 2\pi V_s / \Phi_0$, which is able to excite this $L_s C_s$ circuit. This generates an alternating voltage with frequency $\omega_{L_s C_s} = 1/\sqrt{L_s C_s/2}$ and thus, causing the appearance of Shapiro steps for whether $\omega_J = n\omega_{L_s C_s}$ or

$$V_{r,n} = n \frac{\Phi_0}{2\pi \sqrt{L_s C_s/2}} \quad (n \in \mathbb{Z}) \quad (2.76)$$

is fulfilled. $V_{r,n}$ describes the necessary voltage for the fulfillment of the resonance condition, i.e. the voltage at which the Shapiro steps occur. This means that measuring the voltage at which those steps occur and knowing the inductance of the SQUID loop, we are able to determine the capacitance of the Josephson junction, assuming that both JJs are identical [Mag81, Mae95]. In order to make the Shapiro steps visible in our measurements, since those steps occur in the subgap area, it is also necessary to suppress the maximal supercurrent running through the unshunted SQUID. For this, as indicated in Figure 2.12, a Helmholtz coil is generating a magnetic flux inside the SQUID loop, which modulates the maximal supercurrent. If the applied flux is $\Phi_s = (m + 1/2)\Phi_0$ with $m \in \mathbb{Z}$, then the maximal supercurrent is at its minimum. The Shapiro steps become visible if the screening parameter β_L is small enough, such that the suppression of the supercurrent is sufficient to make the first current step at the voltage $V_{r,1}$ visible. This measurement method was used to estimate the JJ capacitance of one of the JJs fabricated within the framework of this thesis, see section 4.3.

3. Experimental Methods and Results

In the following chapter, we introduce the methods of fabricating Nb/Al-AlO_x/Nb based Josephson junctions as well as optimising the tri-layer deposition and present the measurement technique to record the *IV*-characteristics of the JJs in order to check their quality. In the framework of this Master thesis, we further pushed the transition of window-type based Nb/Al-AlO_x/Nb JJs towards the cross-type based ones (CrossJJ) in our group. In this chapter, we motivate the advantages of CrossJJs and provide details of the microstructuring processes. In addition, we will show our approach to optimise the quality of our in-house junction fabrication by conducting quality checks of our in-house sputter-deposited niobium films and oxidized aluminium layers. Lastly, we will show the method of analysing our data to determine the critical current, defined for $T = 0\text{ K}$, from the *IV*-characteristics measured at $T = 4.2\text{ K}$.

3.1 Fabrication Process of Nb/Al-AlO_x/Nb Junctions

As we have seen in previous chapters, JJs are the basic and most critical elements of many superconducting devices. It is therefore desirable to have a reproducible wafer-scale fabrication yielding JJs with a uniform and high production quality. The photolithographic steps used for the microfabrication are, next to material and geometry choices, very critical in this regard. Until recently, the SQUIDs produced in our research group have been based on the window-type geometry with Nb/Al-AlO_x/Nb based junctions [Bau22]. In the following we show the key differences between the cross-type and window-type junctions and why it is reasonable to switch production to cross-type based SQUIDs. The used facilities for fabrication we mention in the following, are explained in detail in subsection 3.1.4.

3.1.1 Capacitance of Josephson Junctions

In the framework of the RCSJ-model, a JJ is modelled as a plate capacitor due to a thin insulating barrier being sandwiched by two metal "plates". The intrinsic capacitance C_{JJ} of a junction depends on the insulating barrier and therefore on the oxidation parameters, just like the critical current density j_c . Because of this co-dependence, there is a functional relationship that describes how a change of

the critical current density affects the intrinsic capacitance. Specifically for Nb/Al_xO/Nb based junctions, the equation

$$\frac{1}{C'_{JJ}} = a - b \ln(j_c) \quad (3.1)$$

with constants a and b that depend on processing parameters and the intrinsic capacitance per area C'_{JJ} , was able to model this co-dependence [Mag81, Mae95]. The JJ capacitance C_{JJ} as well as the critical current I_c scale directly with the junction area A . Reducing the capacitance of the junction by reducing the area leads to a reduction of the critical current. To maintain the desired critical current, the critical current density has to be increased by reducing the junction thickness. This would then lead to an increase of the capacitance, described by Equation 3.1. Nevertheless, due to the weak, logarithmic dependency, a reduced junction area is favourable. This moves the resonance frequency $f_{LC} = 1/(2\pi LC)$ of the LC -circuit, which is inevitably part of the dc-SQUID, away from the operation frequency $f_{op} = 0.3 f_J$ [Ryh89] and reduces the fundamentally achievable energy sensitivity $\varepsilon \propto \sqrt{LC}$, see Equation 2.71.

3.1.2 Window-type Josephson Junction

The current standard of JJ production in this research group is schematically sketched in Figure 3.1 and a picture taken with a scanning electron microscope in Figure 3.2. It starts off with the cleaning of the thermally oxidised Si-substrate by the *in-situ* ion

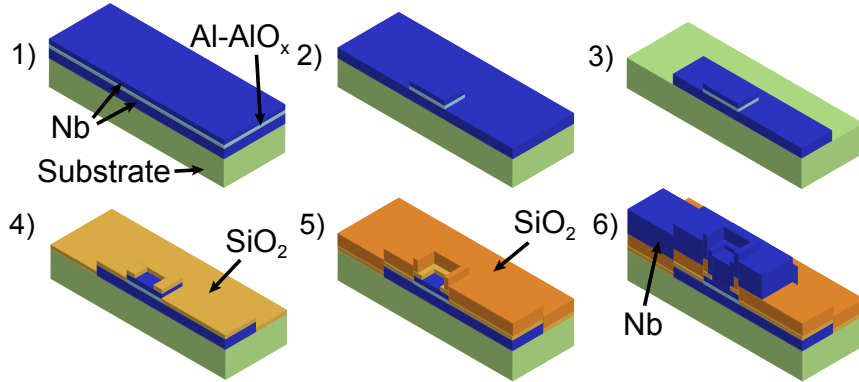


Figure 3.1: Schematic depiction of window-type JJ fabrication. 1) *In-situ* deposition of the tri-layer structure Nb/Al-AlO_x/Nb. 2) Structuring top electrode and insulation barrier. 3) Structuring bottom electrode. 4) Deposition of first SiO₂ layer. 5) Deposition of second SiO₂ layer. 6) Structuring the Nb contacting layer by a lift-off process. Adapted from [Bau22].

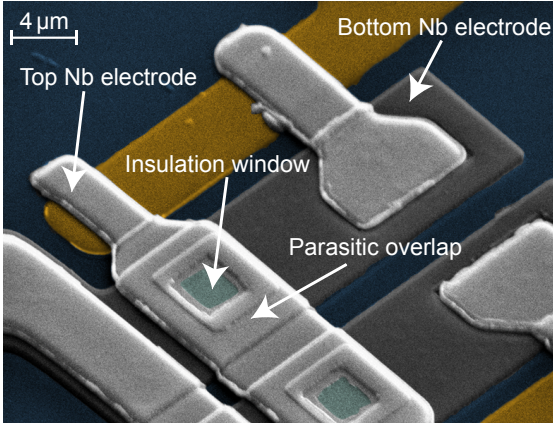


Figure 3.2: Scanning electron microscope picture of a window-type JJ that was built with the process described in Figure 3.1. From [Bau22].

gun etching inside the load lock of our UHV-sputtering system¹ to prepare the wafer for the subsequent Nb/Al-AlO_x/Nb tri-layer deposition. Deposition of the tri-layer takes place *in-situ* inside the sputter chamber by successively sputtering 250 nm Nb and 20 nm Al. Before the last Nb layer of the tri-layer is deposited, the Al layer is exposed to an O₂ atmosphere. The oxidation pressure p_{ox} and time t_{ox} are crucial for the oxidation step and determine film properties like the critical current density j_c of the insulating AlO_x barrier, which will be discussed in-depth in subsection 3.2.3. Once the Al layer is oxidised, the top Nb layer of the tri-layer is sputtered on top with a thickness of 125 nm. In the next step, the top electrode is structured by firstly applying a photoresist mask for which the UV-sensitive positive photoresist AZ MIR 701² is used and is structured by being exposed by an MLA 150³ laser lithograph. The now uncovered parts of the underlying top Nb layer are dry etched with an ICP-RIE⁴ dry etch process using an SF₆/Ar atmosphere for which we used the Oxford PlasmaPro 100 Cobra⁵. The Nb etch is then followed up by dry etching the Al layer, at which point the structure of the top electrode is completed. Analogously to the top part, the bottom electrode gets structured by dry etching. In order to galvanically insulate the bottom electrode from Nb-strips of the contacting layer crossing, see step 6) in Figure 3.1, two insulating SiO₂ layer thicknesses of 125 nm and 250 nm are rf-sputter deposited. These isolating layers are structured via a lift-off process using a negative photoresist. This step, as seen in 5) of Figure 3.1, is what determines the size of the junction area, as a window-like opening is created for contacting the top electrode with a 600 nm Nb layer that is also structured with a negative photoresist.

¹PreVAC sp. z o. o., Raciborska Str. 61, PL-44362 Rogów, Poland

²Merck Performance Materials GmbH, Rheingaustraße 190, 65203 Wiesbaden, Germany

³Heidelberg Instruments Mikrotechnik GmbH, Mittelgewannweg 27, 69123 Heidelberg, Germany

⁴Inductively Coupled Plasma-Reactive Ion Etching

⁵Oxford Instruments Plasma Technologies, North End, BS49 4AP Yatton, Bristol, United Kingdom

These window-type JJs have shown to be quite reliable in terms of reproducibility of high quality SQUIDs. This can, for example, be seen in the scalability of the normal resistance R_n and the critical current I_c with the junction area as well as in the comparably high resistance ratio R_{sg}/R_n [Kem13, Zim18]. Nonetheless, alignment inaccuracies of the junction window limit the reachable junction area to sizes of around $3.5\text{ }\mu\text{m} \times 3.5\text{ }\mu\text{m}$. Important to note here is that the window in the insulation layer has an edge length of $2\text{ }\mu\text{m}$. Another inherent challenge for this type of process is the unavoidable creation of parasitic overlaps of the bottom and the contact electrode causing a parasitic contribution to the junction capacitance, also seen in Figure 3.2 and step 6) of Figure 3.1.

3.1.3 Cross-type Josephson Junction

To overcome these limitations in the window-type fabrication, the cross-type JJ fabrication process was introduced in a previous work [Bau22] with which we are able to reach edge lengths down to $1.0\text{ }\mu\text{m}$, reduce the junction area and minimise the parasitic overlaps. As the name of this type of junction already suggests, the junction is defined by the crossing of a Nb and a tri-layer strip, i.e. a Nb/Al-AlO_x/Nb layer, as shown in Figure 3.4 in form of a optical microscope and scanning electron microscope picture. Figure 3.3 shows schematically the fabrication steps of a CrossJJ. As for the

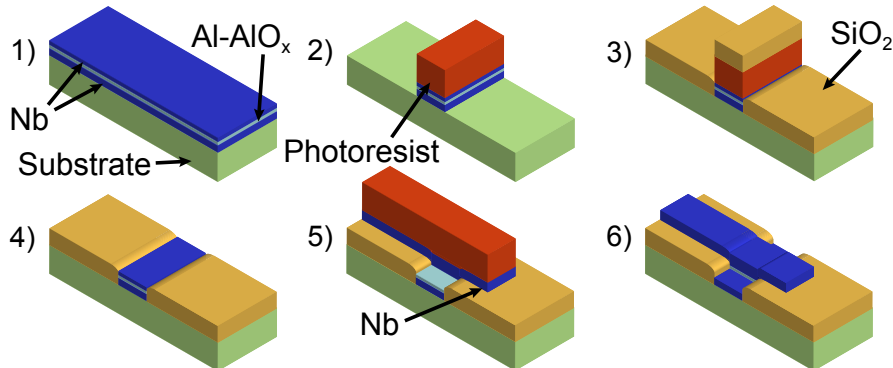


Figure 3.3: Sketch of the cross-type JJ fabrication processes that was used in the framework of this thesis. 1) In situ deposition of the tri-layer structure Nb/Al-AlO_x/Nb. 2) Structuring the tri-layer to form a stripe, leaving the photomask for the next step. 3) Depositing SiO₂ over the whole wafer for planarisation and to insulate the bottom Nb electrode. 4) Lifting the photomask off to uncover the tri-layer stripe underneath. 5) Depositing and structuring of the top Nb electrode to form a stripe perpendicular to the tri-layer stripe. 6) Etching away the uncovered AlO_x layer and lifting the residual photoresist. Adapted from [Bau22].

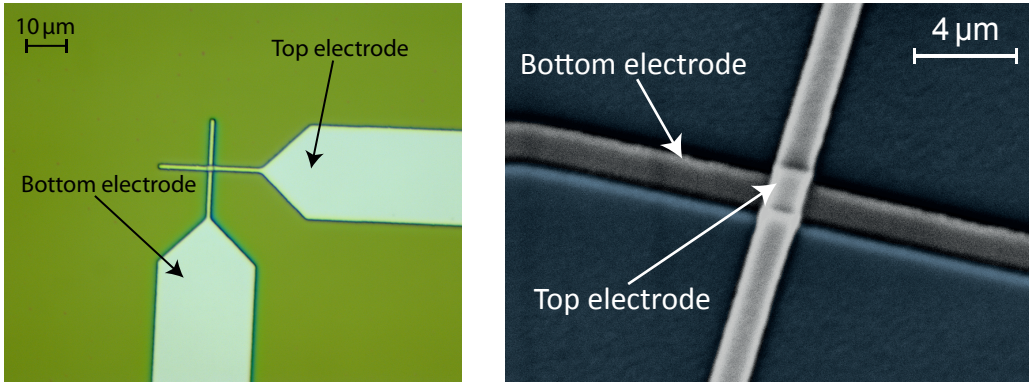


Figure 3.4: Left: Snapshot taken with an optical microscope of a cross-type JJ with an area of $1\text{ }\mu\text{m} \times 1\text{ }\mu\text{m}$ that was fabricated with the process described in Figure 3.3 within the framework of this thesis. Right: Scanning electron microscope picture of a cross-type JJ with an area of $2\text{ }\mu\text{m} \times 2\text{ }\mu\text{m}$, taken from [Bau22].

window-type JJ fabrication, we start off with a wafer-scale deposition of a Nb/Al-AlO_x/Nb tri-layer on a thermally oxidised Si substrate. The thickness of the bottom and top Nb layer were chosen to be 100 nm each and the tunnel barrier thickness was varied between 7 nm and 14 nm for optimization purposes, see chapter 4. The Al layer was again oxidised with a pressure $p_{\text{ox}} = 33.33\text{ mbar}$ for a time $t_{\text{ox}} = 15\text{ min}$ such that the desired critical current density is reached. Afterwards a stripline is structured by utilising the positive photoresist AZ MIR 701 that serves as a mask for the ICP-RIE dry etch process. This way the only limitation for the structure size is the resolution of the laserlithograph MLA150 and we are able to go down to line widths of 1 μm. The etching of the tri-layer itself is divided into three steps: first, the top Nb layer is dry etched down to the Al-AlO_x layer, which serves as an etch stop, using a mixture of SF₆ and Ar as etchant, then the insulation layer is chemically wet etched using an acid containing 16 H₃PO₄ : 1 HNO₃ : 1 CH₃COOH : 2 H₂O and analogously to the top Nb layer, the bottom Nb layer gets dry etched as well. In order to avoid short circuits between the later deposited Nb-contact layer and the bottom electrode as well as enabling an as planar as possible deposition of further layers, a 200 nm thick SiO₂ insulation layer is deposited, whose height should guarantee to cover the bottom Nb and Al-AlO_x layer. We would like to stress that all these structuring steps are performed with the same photoresist mask, hence overcoming any alignment limitations. Nonetheless, due to the height of roughly 1.6 μm of the photoresist mask, a shadow is created during SiO₂ deposition that is cast over a close proximity of the tri-layer-line. This shadow causes the formation of long dips all along the tri-layer-line on both sides, as seen in 3) to 6) of Figure 3.3, and is in the case of our in-house deposition static, due to the substrate not being rotated during deposition. Fortunately, this does not pose a problem as long as the side walls

of the bottom electrode and barrier layer are covered. Furthermore, the chemical wet etch process to remove the Al/AlO_x with a mixture of acetic, phosphoric, and nitric acid has the benefit of passivating the side wall of the bottom and top electrode. During this wet etching, the nitric acid converts the Al surface into aluminium oxide which then gets dissolved by the phosphoric acid. The acetic acid and water inside the mixture are used to regulate the PH value and the etch rate. Hereby, the nitric acid not only affects the aluminium but also the niobium which then gets oxidized as well but not dissolved. This way, the edges of the junction get an additional oxide barrier a few nm thick, thus improving the insulation of the tri-layer stripe [Bau22].

After dissolving the resist and lifting off the residual SiO₂, a 250 nm thick Nb layer is deposited all-over the wafer and structured by using a AZ MIR 701 resist mask for the ICP-RIE dry etch. This contacting layer is structured in form of lines that are oriented perpendicular to the tri-layer line. The subsequent dry etching step removes the exposed Nb (from both layers, the contacting and the top layer) while the underlying SiO₂ and Al-AlO_x layers serve as an etch stop. The now exposed Al layer gets chemically wet etched and the actual junction is defined by the cross section of the intersecting tri-layer- and Nb-lines. Thus, the upper lying Nb is not only the top electrode but also the contacting layer and the lower lying Nb is the bottom electrode as well as contacting layer.

Compared to the window-type fabrication, this method of producing cross-type geometries is significantly simpler and only requires two photolithographic steps for completion. Due to the cross-type structure, the alignment accuracy of the laser-lithograph does not pose a limitation for the JJ area anymore since it only matters whether the stripes overlap. Furthermore, any kind of parasitic overlap is completely avoided for cross-type junctions, and therefore the capacitance of every junction is determined by its intrinsic contribution. The area of the cross-type Josephson junctions is limited by the combined resolution of the photoresist and laserlithograph. It was already shown in a previous work of our research group [Bau22] that we are able to produce JJ areas below 1 μm². This reduced area does not only reduce the intrinsic capacitance and hence increase the device performance, but, for a given critical current, also reduces the oxidation time significantly compared to window-type fabrication.

3.1.4 Facilities at Kirchhoff-Institute for Physics

The sputtering system by PreVAC used within the framework of this thesis is an ultra-high vacuum (UHV) system consisting mainly of two chambers, the load lock and the sputter chamber. Both chambers are pumped by turbomolecular pumps and reach a base pressure of $\sim 2 \cdot 10^{-8}$ mbar. The sputter chamber is equipped

with seven dc-powered magnetron sputter guns of which six are confocally oriented around the centre of the chamber and the remaining one oriented in parallel to the horizontally rotating substrate holder at the centre of the chamber. The confocally oriented sputter guns contain target materials of 2 inch diameters while the parallel oriented sputter gun is of 4 inch diameter. The target materials used within the framework of this thesis were Nb with which we are able to achieve a sputtered film homogeneity of 2.3 % at 50.8 mm diameter, and Al with which we are able to achieve a sputtered film homogeneity of 3.9 % at 50.8 mm diameter. In order to compute the homogeneity of films, one has to measure the film thickness y at different distances x from the centre of the deposited film, with the centre point defining the zero point, and then fit a polygon of second degree $f(x)$ to the measured data $y(x)$. Then the homogeneity at 50.8 mm is calculated, as defined within this research group, by taking the relative height difference between the fit values at centre point and the point at 25.4 mm and dividing that by the fit value at the centre point: $|[f(0 \text{ mm}) - f(25.4 \text{ mm})]/f(0 \text{ mm})|$.

The load lock serves as a means of loading the wafer without breaking the UHV in the sputter chamber as well as cleaning the substrate with an ion gun before processing it further in the sputter chamber. The process gases used within the PreVAC sputtering system are Ar with a purity of 99.9999 % and O₂ with a purity of 99.998 %.

For the fabrication of a Nb/Al-AlO_x/Nb tri-layer, a 3 inch sized thermally oxidised Si-substrate is pinned onto a substrate holder containing cooling pins to cool down the substrate from below with a water cooling system during sputtering. After the load lock is evacuated, the substrate is cleaned by etching it with an ion beam for 1 min at an Ar flow rate of 10 sccm and accelerating voltage $U = 400 \text{ V}$. After loading the substrate into the sputter chamber, Nb is sputter-deposited by means of the 4 inch sized dc-magnetron at pressures between 3 μbar and 7 μbar and a power of $P_{\text{Nb}} = 700 \text{ W}$. We obtain a nearly pressure-independent sputtering rate of $\sim 40.1 \text{ nm/min}$. Right after that, Al is sputter-deposited by utilising the 2 inch sized, at an angle of 32.5° confocally oriented dc-magnetron at an Ar pressure of 4 μbar and a power of $P_{\text{Al}} = 450 \text{ W}$, for which we reach a sputtering rate of 31.5 nm/min. To prepare the load lock for the oxidation of the Al film, the load lock is flushed for 10 min with O₂ at a pressure of 10 mbar. After evacuating the load lock once again, the substrate is loaded back into the load lock where it gets oxidised for $t_{\text{ox}} = 15 \text{ min}$ at a pressure $p_{\text{ox}} = 33.33 \text{ mbar}$. After oxidation of the Al-layer, the load lock gets evacuated and the substrate transferred back to the sputter chamber, where the top Nb-layer gets deposited with the same parameters as the first Nb-layer. In the framework of this thesis, the thickness ratio of the Nb/Al-AlO_x/Nb tri-layers were varied to be 100 nm/ x nm/100 nm with $x = 7, 10, 14 \text{ nm}$, see also chapter 4.

The deposition of the contacting Nb-layer was also conducted in the PreVAC sputtering system and was chosen to be 250 nm thick. Before deposition, the wafer is cleaned by ion gun etching in an Ar atmosphere for 1 min to remove the oxide layer of the previously deposited Nb-layer to guarantee a superconducting electrical contact.

For the deposition of the SiO_2 layer, the Alcatel SCM 601 sputtering system⁶ was used, such that the other targets, used for deposition, do not get contaminated by the processing gases used for SiO_2 sputtering. Here, a process gas mixture of Ar and O_2 in a ratio of 60 : 40 is let into the sputter chamber at a pressure of $p_{\text{Ar},\text{O}_2} = 0.7 \text{ Pa}$ and an rf-plasma is ignited by a 3 inch magnetron containing the SiO_2 target with an applied power of $P_{\text{SiO}_2} = 250 \text{ W}$. The resulting sputtering rate is $\sim 2.36 \text{ nm/min}$.

As mentioned in subsection 3.1.3, the structuring steps of the Nb layers utilised dry etch processes for which we used the Oxford PlasmaPro 100 Cobra. Here, a mixture of SF_6 and Ar is let in, in a flow-rate ratio of 20 sccm/10 sccm. The ICP-power is adjusted to be 300 W and the HF-power is adjusted to be 10 W.

3.2 Optimisation of Trilayer Deposition

The most critical steps that determine the quality of a Josephson junction are the deposition steps of the tri-layer and the *in-situ* oxidation step of the Al before the deposition of the Nb top electrode [Ima92b, Ima92a, Du07b, Du07a]. As such, we present in the following section the steps we took to ensure the deposition of a high quality tri-layer.

3.2.1 Stress Measurement

The deposition of metal films on substrates generates stress, not only on the substrate but also the film itself. Extreme stress can cause deformation, cracking, shorts or other failures that will render the junctions dysfunctional. It is of interest to not only have a reliable fabrication but to also have a high quality of the fabricated junctions. It has been shown that it is favourable to have a completely stress-free or slightly compressive Nb film to achieve the best superconducting properties as well as the best junction properties [Ima92b, Ima92a, Du07b, Du07a].

All stress measurements within this thesis have been carried out with a Dektak XT profilometer⁷. Here, the substrate's curvature prior to the deposition gets measured and then again, along the same trace, after deposition. The analysis software of the

⁶Alcatel Vacuum Technology France SAS, part of Pfeiffer Vacuum SAS by now, 98 Avenue de Brogny, 74009 Annecy, France

⁷Bruker Corporation, 40 Manning Rd, Billerica, MA 01821, United States

profilometer uses the bending plate method [Sto09, Jac66] to compute the stress of the deposited film. Parameters for this calculation are the radius of curvature of the substrate before and after deposition as well as material properties of film and substrate, namely the crystal orientation of the substrate and the thickness of substrate and film. Expressing the height of the substrate as a twice continuously differentiable function of distance along the substrate, $h = f(x)$, the radius of curvature is given by:

$$R(x) = \frac{(1 + h'^2)^{\frac{3}{2}}}{h''}. \quad (3.2)$$

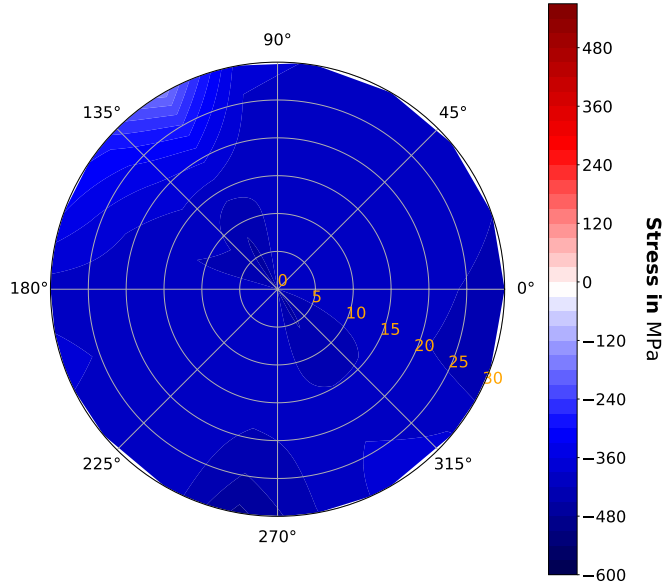
If we assume that the substrate is completely flat before deposition, then the stress is given by

$$\sigma = \frac{1}{6} \left(\frac{1}{R_{\text{post}}} - \frac{1}{R_{\text{pre}}} \right) \frac{E_Y}{(1 - \nu)} \frac{t_s^2}{t_f}, \quad (3.3)$$

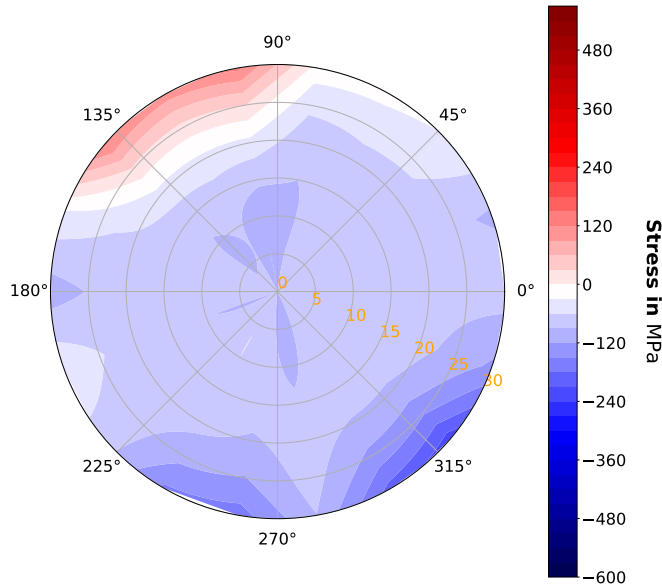
where R_{pre} , R_{post} are the radii of curvature before and after deposition respectively, $E_Y = 169 \text{ GPa}$ is Young's modulus of the silicon wafer, $\nu = 0.279$ its Poisson's ratio, $t_s = 381 \mu\text{m}$ is the substrate thickness and t_f is the film thickness, which was chosen to be 200 nm and 100 nm for the stress tests.

3.2.2 Minimizing Nb Film Stress

As previously mentioned, one wants to have either a stress-free or slightly compressive film for high quality junctions. For a given substrate, the stress that the deposited Nb film transfers on it heavily depends on the thickness of the film and the parameters during deposition. Since the thickness is usually fixed by design considerations, minding the magnetic penetration depth as well as the fact that stress is the highest for very thin films, we decided to measure 200 nm thick films and minimise the stress for films in this range of thicknesses. The parameter space in which we are supposed to find an optimum, consisted mainly of two variables: the pressure p of the process gas Ar and the power P of the sputtering source. In the PreVAC sputtering system two different Nb targets were installed, a 2 inch diameter target that was confocally oriented in a 30° angle and a 4 inch one which was right above the substrate holder. Tests with films deposited by the 2 inch target have shown that regardless at which point we are in parameter space, we not only had T_c values that deviated strongly, up to 22% from the expected bulk value of 9.25 K, but also always yielded tensile stresses over the whole parameter space which was accessible to us. The reason for this might stem from the confocal geometry as well as the low upper power bound of 300 W, due to the melting temperature of materials in the vicinity of the target inside the sputtering gun and the small diameter of the target. These issues lead to a lower sputtering rate as well.



(a) Sputtering parameters: Ar pressure $p = 3.5 \mu\text{bar}$, sputtering source power $P = 700 \text{ W}$



(b) Sputtering parameters: Ar pressure $p = 6.5 \mu\text{bar}$, sputtering source power $P = 700 \text{ W}$

Figure 3.5: 2D Stress maps of the central 60 mm of a 3-inch Si-Wafer with 200 nm Nb deposited on it. For the deposited Nb we used the 4inch target with planar geometry. The orange ticks show the radial distance from the centre in mm. Negative stress values (blue) show compressive stress while positive stress values (red) show tensile stress. The average stress up to a radius of $r = 20 \text{ mm}$ are a): $\sigma = -(412 \pm 13) \text{ MPa}$ and b): $\sigma = -(79 \pm 12) \text{ MPa}$.

For this reason we switched to the larger 4 inch Nb-target, oriented in parallel to the substrate, for which a sweet spot in parameter space had already been adjusted by a different member of our research group.

Still, the stress measurement that had been performed for this target before was done by examining how the 200 nm thick Nb film coils when lifted off a photoresist. This is rather imprecise, since film growth and stress build-up behaves vastly different on photoresist than on a thermally oxidised Si substrate, which is why we firstly investigate what the difference would be for 200 nm films using the method of stress measurements. This can be seen in the stress map of a wafer in Figure 3.5 a), which was fabricated with the old optimised parameters, showing a strong compressive stress of $\sigma \approx -412 \text{ MPa}$ and in Figure 3.5 b) with the newly optimised parameters, confirming that the previous method was not reliable enough. These stress maps were generated by nine lines of measurements with the Dektak XT profilometer across the wafer in angle steps of 20° . The filled contour plot was done via Python using the

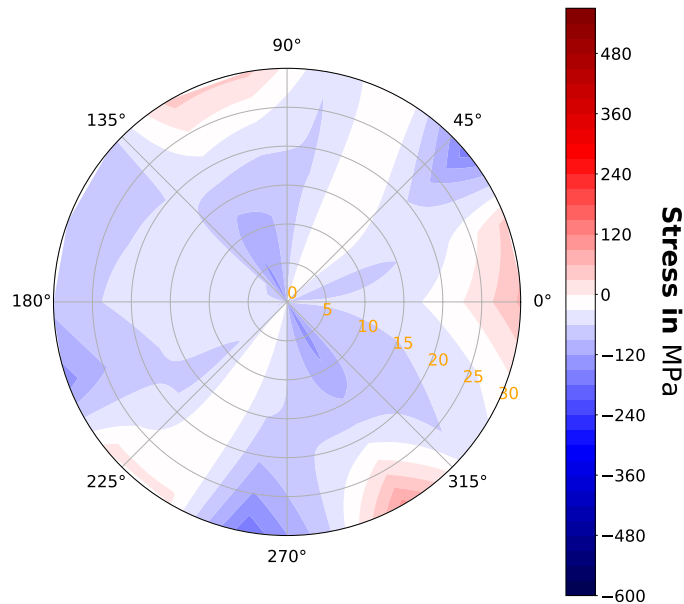


Figure 3.6: 2D Stress map of the central 60 mm of a 3-inch Si-Wafer with 100 nm Nb deposited on it. The sputtering parameters were: Ar pressure $p = 5 \mu\text{bar}$, sputtering source power $P = 700 \text{ W}$. The orange ticks show the radial distance from the centre in mm. Negative stress values (blue) show compressive stress while positive stress values (red) show tensile stress. The average stress up to a radius of $r = 20 \text{ mm}$ is $\sigma = -(59 \pm 28) \text{ MPa}$.

matplotlib library, which utilised the marching squares algorithm⁸. The blue colour indicates a compressive stress, the red colour a tensile stress and the white colour the stress-free case. Increasing the Ar process gas pressure for Nb deposition to 6.5 µbar, helped to strongly decrease the stress of the deposited Nb film, as can be seen in Figure 3.5 b). Since the targeted thickness for the bottom and top electrode for the tri-layer deposition was 100 nm, characterization measurements were also done for such thinner films, and indeed the sputtering parameters for stress-free films are slightly different, as shown in Figure 3.6. It is worth to notice that the critical temperature of all films that were sputtered with the planar geometry is close to $T_c = 9.2$ K, i.e. only less than a percent away from the bulk value of Nb with $T_c = 9.25$ K, which is an additional indicator of the high quality of the deposited films. It is important to mention, that if a target is worn out due to repetitive use, the optimal process parameters for stress-free deposition changes significantly. It is therefore recommended to exclusively use a Nb target for tri-layer deposition such that the optimisation has not to be repeated too frequently.

For the sputtering of 200 nm films, we slightly increased the Ar-pressure from 6.5 µbar to 7 µbar such that the compressive stress is further reduced. This point in parameter space was not measured in order to not waste further substrates.

3.2.3 Aluminium Thickness and Oxidation

The most critical part of tri-layer deposition as well as the general functioning of Josephson junctions is the tunnel barrier. The quality of the Al-AlO_x barrier on Nb has been already extensively studied before, and we will therefore only present the results of these previous works [Ima92a, Du07a, Tsu93] and utilise them in our junction fabrication process. Nonetheless, we note that these previous projects did not use a confocally arranged sputtering source for Al deposition as we did. As such, the findings we present are just a starting basis for our optimisation of the deposition. The quality of tunnel barriers depend on the surface coverage, the interfacial diffusion, the thickness, the composition, the integrity and uniformity of the barrier itself, including the flat bottom Nb electrode, with the surface coverage and uniformity being the most critical and necessary part for the functioning of a Josephson junction.

Looking at the thickness of the Al-layer, experiments have shown [Ima92b] that there is a lower boundary of roughly 1.4 nm in order to completely wet the bottom Nb electrode, otherwise it will be partially exposed to air causing the formation of Nb₂O₅ on the surface of the Nb as well as NbO_x suboxides. For elemental Al, thicknesses

⁸For further references, see CountourPy documentation: <https://contourpy.readthedocs.io/en/v1.0.7/>

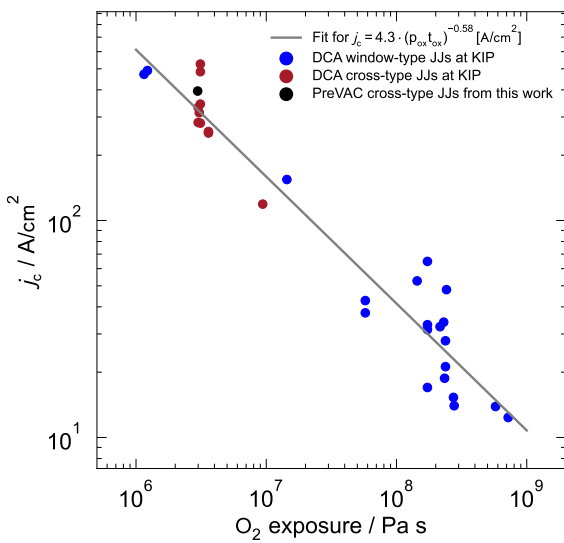


Figure 3.7: Critical current density j_c plotted against the oxidation parameter product $t_{\text{ox}} p_{\text{ox}}$. The black point indicates the first recorded critical current density of JJs fabricated, using the PreVAC sputtering system within the framework of this work. The purple and red points indicate window-type and cross-type JJs that have been produced in the older DCA sputtering system⁹. “KIP” in the legend of the plot stands for “Kirchhoff-Institute for Physics” and indicates data points determined in previous works in the cleanroom of that institute.

larger than 2.8 nm underneath the Al-oxide, the Aluminium acts as a diffusion stop for oxygen from the above lying Al-oxide. For clean interfaces with no suboxides, it is therefore necessary to have a Al thickness of at least 2.8 nm. An upper boundary is given by the decreasing gap voltage of junctions with an Al tunnel barrier thicker than 10 nm, which is due to the stronger occurring proximity effect, since the thickness of the oxidised part stays constant while the elemental part becomes thicker.

Significant for the coverage of Al on Nb is the quality of the underlying Nb film as well as its thickness and roughness. The surface coverage seems to deteriorate for increasing Nb thickness with the biggest changes appearing at Nb deposited at higher Ar pressure. For Nb thicknesses larger than 100 nm, a significant degradation of the junctions *IV*-characteristics sets in and for too thin films, the superconducting features of the Nb film degrade as well, causing a decrease of the gap voltage of Josephson junctions [Ima92b, Du07b].

The conclusion is therefore to deposit a 100 nm thick Nb film, thick enough to be above the magnetic penetration depth, at low Ar pressure with a 7 nm thick Al film on top in order to guarantee a high quality junction. As for the oxidation parameters, it is empirically known that the critical current density j_c of the tri-layer is proportional to $(t_{\text{ox}} p_{\text{ox}})^{-\kappa}$ with κ being an exponent that needs to be experimentally determined for the specific sputtering system used [Kem13]. With the oxidation parameters that have been used in tests of cross-type JJ fabrication before in our research group but in a different sputtering system [Bau22], we find that the current density for the chosen parameter is very close to the previous points, as seen in Figure 3.7. Nonetheless, we note that for a full and more precise characterisation

of the oxidation behaviour of the PreVAC sputtering system, more data points are required.

3.3 Characterisation of Josephson Junctions

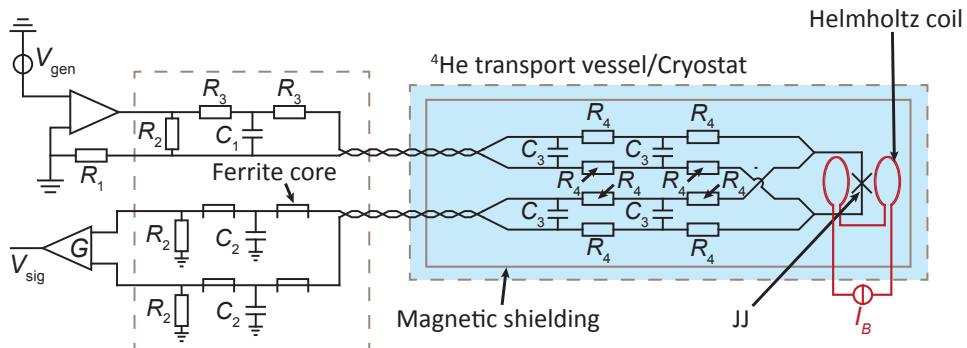
During the optimisation processes, multiple charges of wafers with cross-type JJs were produced for which process parameters as well as process steps were adjusted accordingly in order to yield JJs with a reproducible and uniform high quality as well as a small parameter spread. Each wafer contained 192 chips, each equipped with eight junctions with edge lengths ranging from $1\text{ }\mu\text{m}$ to $4.2\text{ }\mu\text{m}$ as well as four unshunted SQUIDs with junction edge lengths of $2\text{ }\mu\text{m}$. Four different chips were designed with only the enclosed area of the unshunted SQUIDs varying. As a first step, the quality of the JJs themselves was tested by recording their *IV*-characteristics via a four-terminal sensing setup and extracting the relevant characteristic quantities in order to judge their quality and draw conclusions about the tri-layer and tunnel barrier quality.

3.3.1 Four-wire Sensing

For the four-wire sensing, we used a setup that is sketched in Figure 3.8. The chip to be tested, was glued onto a circuit board and then electrically contacted with Al bonding-wires. The circuit board was mounted on a dipstick and connected to a filtering circuit board containing low-pass filters. The part of the dipstick that had the chip mounted on, was additionally shielded by a cryoperm as well as niobium shield to block unwanted external magnetic fields. The dipstick itself was put into a 1001 transport-vessel of liquid helium to cool the Josephson junctions down to 4.2 K , such that the niobium was superconducting with a relatively low quasi-particle density due to $T < 0.5 T_c$. In order to generate a current I , we used a waveform generator which was converted into a differential voltage V_{gen} by an instrumentation amplifier and connected to an effective resistance R_{gen} . This generator was set to send a low frequency triangle signal in order to get the full characteristic behaviour of the junction for positive and negative currents. The effective resistance consists of all resistances of the input circuit connected in series and defines with the generated voltage a current of

$$I = \frac{V_{\text{gen}}}{R_{\text{gen}}} = \frac{V_{\text{gen}}}{R_1 + 2R_3 + 4R_4 + R(V)}. \quad (3.4)$$

⁹DCA Instruments Oy, Aerotie, 20360 Turku, Finland



$$R_1 = 1\Omega, \quad R_2 = 10\text{M}\Omega, \quad R_3 = 5.1\text{k}\Omega, \quad R_4 = 51\Omega, \quad C_1 = 33\text{pF}, \quad C_2 = 1\text{nF}, \quad C_3 = 47\text{nF}$$

Figure 3.8: Circuit of the experimental setup for measuring the *IV*-characteristics of Josephson junctions. For measurements of Shapiro steps or Fraunhofer patterns, the chip was mounted in the centre of a Helmholtz coil.

Here, $R(V) = V/I$ describes the voltage-dependent resistance of the Josephson junction while the other resistances are part of the filter elements, as seen in Figure 3.8. Next to the mentioned resistances, a capacitor was connected, working as an RC low-pass filter together with the resistances, and an additional high-impedance resistor was used. This apparatus was connected to the filtering circuit boards of the dipstick via twisted CuNi¹⁰ wire pairs. The other two wires, that made up the four-wire sensing, were used to measure the voltage drop across the junctions. For this we also used a twisted CuNi wire pair, which was connected with the output of filtering box. The output contained a LC low-pass filter as well as a high-impedance resistance connected to ground for each wire. The high-impedance connection to ground was done to prevent electrostatic discharges. Since the voltage signal of the Josephson junctions used in this thesis are rather low, the output signal was amplified by a differential amplifier whose amplifying factor G was adjustable to be 10, 100, 200 or 500. In order to read in and analyse the signals, the junction output signal, the waveform generator signal as well as its synchronizing signal were connected to an analog-to-digital converter¹¹, whose measurement data was read out by a readout program called PAQS, previously developed by our research group [Hen17]. The additional measurement of the synchronizing signal was performed to avoid a significant time delay between the input and output measurement of the junction. The data was then plotted and features were extracted by using an analysing script written in Python, which was developed within our group and extended within this

¹⁰200 µm diameter

¹¹SIS3316-DT 16 Channel Digitizer, Struck Innovative Systeme GmbH, Harksheider Straße 102, 22399 Hamburg

work. This analysing script includes the correction of the measured data necessary due to the finite resistance of the JJ. Since the current I applied is dependent on the total resistance including the JJ resistance, the current I needs to be corrected in the analysis.

3.3.2 Critical Current Determination

As mentioned in subsection 2.2.3, for finite temperatures, the critical current I_c and the current I_{sw} at which the junction switches to the voltage state is not the same. The switching can already occur at a smaller current due to the thermal noise of quasi-particles of the junction resistance and is therefore a statistical quantity. In order to determine the critical current, we use a method which utilises the relation between the gap current I_{gap} and the critical current I_c , that has first been used in our group in the work of [Bau22]. The relation $I_c = \kappa I_{gap}$ [Lik79] is assuming that there is a homogeneous distribution of the critical current density and can therefore be determined by picking out some representative junctions of a wafer, measure the Poisson distribution $P(I_{sw})$ of their switching currents and fit the corresponding theoretical prediction, discussed in subsection 2.2.3.

The distribution of switching currents is measured by measuring the IV -characteristics of a Josephson junction with the experimental setup of Figure 3.8 at $T = 4.2\text{ K}$. For this we generate a current ramp with a peak-to-peak current $I_{pp} > 2I_c$ and a frequency of $f_{gen} = 5\text{ Hz}$. This low frequency was chosen such that it is as far away as possible from the cut-off frequency of our filter elements but still high enough for short measurement cycles. We recorded the IV -characteristics around 3000 times and evaluated the current at which the voltage drop occurs for each of those recordings.

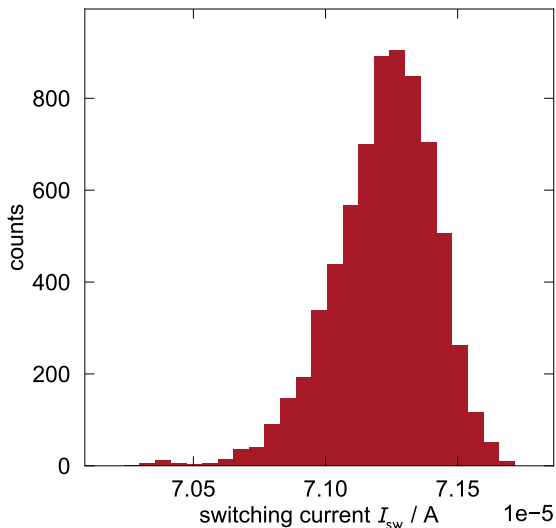


Figure 3.9: Measured switching currents I_{sw} of CrossJJ chip 2A13 of wafer CrossJJ4w13v3 plotted in a histogram. The distribution of switching currents resembles a Poisson distribution.

These switching currents were then plotted in a histogram as shown in Figure 3.9. With the histogram, one can extract the lifetime τ_{th} of the zero-voltage-state and thus the critical current [Dev07]. Looking at the inverse lifetime

$$\tau_{\text{th}}^{-1} = P(I_{\text{sw}}) \left(\frac{dI}{dt} \right) \left(1 - \int_0^{I_{\text{sw}}} P(I) dI \right)^{-1}, \quad (3.5)$$

one can see that for its determination we need the probability density $P(I_{\text{sw}})$, which can be determined by normalising and discretising the histogram in Figure 3.9. Once this is done, the critical current is determined by

$$\left[-\ln \left(\frac{2\pi\tau_{\text{th}}^{-1}}{\omega_0(I)} \right) \right]^{2/3} = \left(\frac{4\sqrt{2}U_J}{3k_B T} \right)^{2/3} \cdot \left(1 - \frac{I_{\text{sw}}}{I_c} \right), \quad (3.6)$$

which results from inserting the approximation $U_0 \approx U_{J0} \frac{4\sqrt{2}}{3}(1-i)^{3/2}$ into Equation 2.41, which assumes $i \rightarrow 1$ [Cas96, Wal03]. With the measured data, the lifetime τ_{th} can be computed and thereof, the left side of the above equation. The right side has the simple structure of a linear equation, which can be fitted to the computed data of the left side. We can therefore obtain a value for the critical current I_c . This calculation process requires multiple iterations, since the left-hand side of the equation contains the plasma frequency $\omega_p = \sqrt{2\pi I_c / \Phi_0 C}$, which is part of $\omega_0(I) = \omega_p(1-i^2)^{1/4}$ and also depends on the critical current as obtained from the

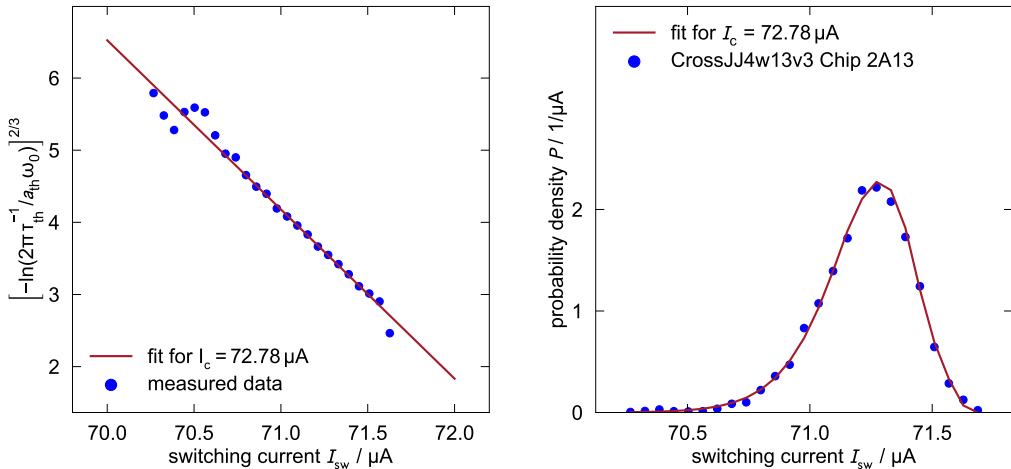


Figure 3.10: Left: normalized inverse lifetime $[-\ln(2\pi\tau_{\text{th}}/a_{\text{th}}\omega_0)]^{2/3}$ plotted against the switching current. The corresponding linear fit determines the critical current I_c . Right: Probability density plotted against the switching current I_{sw} . Taking the fit value of I_c from the left plot, one can see that the corresponding Poisson distribution fits well to the measured data.

right-hand side. Which is why we need to provide a starting value I_c for which we took the maximal value of the measured switching currents I_{sw} . For the capacitance we utilise the empirically determined relation found in [Mae95] between the critical current density and the capacitance of a JJ, see Equation 3.1, and also insert the starting value of I_c . In Figure 3.10 one can see the results for the previous example, which yields a critical current of $I_c = 72.78 \mu\text{A}$ and is, as expected, higher than any recorded switching current due to the finite Temperature of $T = 4.2 \text{ K}$ during the measurement. Since this model seems to fit well to the measured data, one can assume that the early switching to the voltage state is predominantly caused by thermal fluctuations and not by current noise or insufficient shielding of stray electromagnetic fields.

4. Cross-type Nb/Al-AlO_x/Nb Josephson Tunnel Junctions

In order to analyse the quality and wafer-scale homogeneity of the fabricated CrossJJs, we picked chips of different quadrants of the wafers representing every local area of each wafer. For each presented wafer, we varied the thickness of the confocally deposited Al layer to identify the tri-layer with a yield of highest quality JJs. Using the four-wire sensing method, we recorded the *IV*- characteristics of each chip with a maximum of six Josephson junctions per chip, due to our channel limitation of the experimental setup. For each recorded *IV*- characteristics, we extracted the relevant quality parameters, as discussed in section 2.3, and judge them by their relative deviation from the theoretically expected value as well as by their value spread. Here, it should be mentioned that the measurements of the subgap resistances were prone to error due to the rather low resistance of the input circuit compared to the subgap resistance of the Josephson junctions, especially for JJs with small areas. This is due to the fact that we generate the driven current by applying a voltage ramp to a current limiting resistor $R_l = 10.3\text{ k}\Omega$ in series with the JJ, such that the total resistance is influenced by the subgap resistance of the JJ. We therefore exclude the resistance ratio from our discussion, unless the subgap resistance was low enough to be considered to have been measured correctly. In a continuation of this work, it is advisable to adjust the experimental setup by modifying the filter elements such that the cutoff frequency is far enough away from the measurement frequency as well as having a large enough resistance such that the current ramp is not too strongly influenced by the subgap resistance of the JJ.

We start with a showcase of wafers that yielded low quality JJs and discuss the possible reasons. We finish with a full characterisation of the wafer that yielded high quality JJs with an extremely high yield of functioning JJs. An overview of all wafers fabricated within the framework of this thesis is summarized in the appendix in Table I.1. Since the stress optimisation and wafer fabrication were done in parallel due to time reasons, the first three versions of wafers used the optimum Ar pressure of $7\text{ }\mu\text{bar}$ which had been determined for 200 nm thick Nb films. For the later version of wafers, the Nb films were deposited with a lower Ar pressure of $4\text{ }\mu\text{bar}$, as suggested by other publications [Ima92a, Du07b]. The according stress map is shown in Figure I.1 and depicts a compressive average stress of $\sigma = -141\text{ MPa}$. JJ fabrication and tests with Nb deposited at $5\text{ }\mu\text{bar}$ for even less compressive stress, see Figure 3.6, could not be conducted in the timeframe of this thesis anymore.

4.1 Josephson Tunnel Junctions with 7 nm Aluminium and with 10 nm Aluminium

In our first attempt of depositing a tri-layer in the new sputtering system, we aimed for an Al thickness of 7 nm for wafer CrossJJ4w13v1, which seems to be the most optimal value for planar deposited Nb/Al-AlO_x/Nb based Josephson tunnel junctions [Ima92b, Ima92a] in the case of the bottom Nb-electrode having a smooth and flat surface. The Nb-electrodes were each 100 nm thick and the aluminium was oxidised in an oxygen atmosphere of $p_{\text{ox}} = 33.33 \text{ mbar}$ for $t_{\text{ox}} = 15 \text{ min}$ to form the tunnel barrier. Only 12 JJs from different areas of the wafer were tested due to the rather poor quality of the subgap region but all of them were in principle functioning tunnel contacts. Figure 4.1 shows the IV -characteristics of a $1.6 \mu\text{m} \times 1.6 \mu\text{m}$ (design value) CrossJJ on chip 3A3 to give an example of the relatively low junction quality obtained for this thin aluminium thickness of 7 μm . The rather steep curve in the subgap area and therefore very low subgap resistance and resistance ratio of $R_{\text{sg}}/R_{\text{n}} \approx 6.5$ suggest a faulty tunnel barrier that has either defects or is thinner than expected. The missing proximity effect suggests that in the 15 min of oxidation, either the whole Al layer got oxidised, which suggests a thinner than expected layer of Al and/or the surface coverage was insufficient due to the surface of the compressively stressed bottom electrode being too rough, see Figure I.1 in the appendix. This requires further testing by fabricating tri-layers with Nb deposited at an Ar

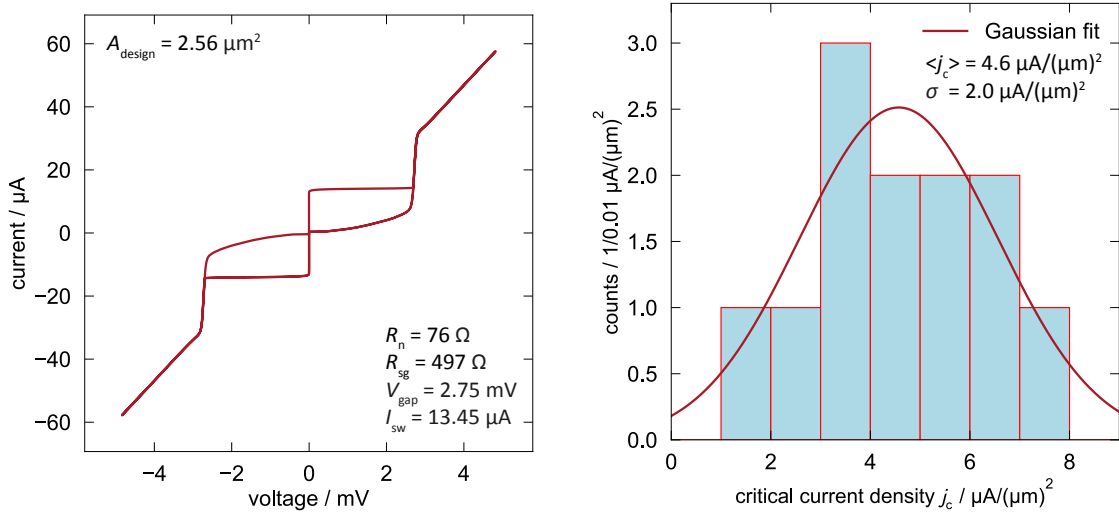


Figure 4.1: Left: IV -characteristics of a CrossJJ with $A_{\text{design}} = 1.6 \mu\text{m} \times 1.6 \mu\text{m}$ of the wafer CrossJJ4w13v1 measured at $T = 4.2 \text{ K}$. Right: Histogram of the critical current density j_c distribution and the corresponding Gaussian fit to determine the mean value and standard deviation.

pressure of 5 µbar, as suggested in Figure 3.6, and further investigation regarding the confocal sputtering of Al and the relative angle of the magnetron sputter gun to the substrate.

In turn, this also suggests that varying the oxidation pressure p_{ox} will not change the expected critical current density, which was in fact observed when comparing CrossJJ4w13v1 with CrossJJ4w13v2, their only difference being the oxidation pressure with the Al layer of CrossJJ4w13v2 being oxidised with $p_{\text{ox}} = 100$ mbar instead, see Table I.1 in the appendix.

Looking at the distribution of the critical current density in Figure 4.1, we can see that the deviation compared to the mean value is rather large with a ratio of $\sigma/\langle j_c \rangle \approx 44\%$. The reason for this could be an inhomogeneous tunnel barrier on wafer-scale, whereby the inhomogeneity could arise from a too thin Al layer that was not able to cover the surface of the possibly rough bottom Nb-electrode. We note here that CrossJJ4w13v1, CrossJJ4w13v2 and CrossJJ4w13v3 were deposited with sputtering parameters which were optimised for 200 nm thin films and as later found out, to be different from the optimal parameters for 100 nm thick films, see Table I.1 and subsection 3.2.2. The sputtered films were therefore most likely tensile such that the flatness of the surface was compromised. All wafers with the ending v4 (indicating the version/iteration) and higher were fabricated after the sputtering system had been opened and the Al target had been moved to another magnetron sputtering gun, which enabled to adjust the angle more freely to increase the sputtering rate of Al from 22 nm/min to 31.5 nm/min. In principle, this change should not have affected the general sputter geometry too much since the distance to substrate and the relative rotation of the substrate holder is still the same. Nonetheless, the ignited plasma and the magnetic fields will not be quite the same as they were previously, such that the deposition behaviour of Al might have changed.

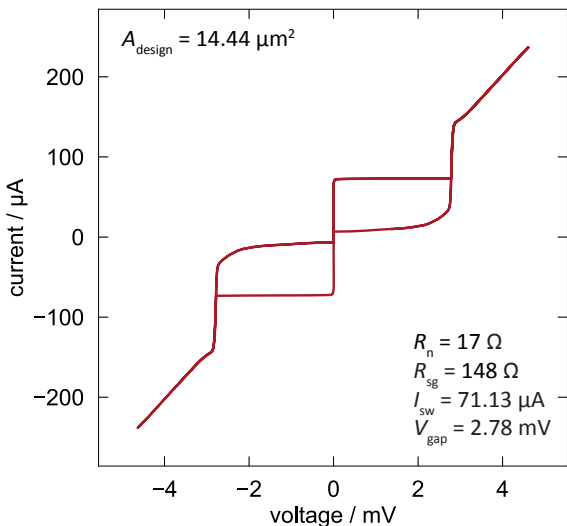


Figure 4.2: *IV*-characteristics of a CrossJJ with $A_{\text{design}} = 3.8 \mu\text{m} \times 3.8 \mu\text{m}$ of the wafer CrossJJ4w13v5 measured at $T = 4.2 \text{ K}$.

Figure 4.2 shows, as an example, the *IV*- characteristics a junction of wafer CrossJJ4w13v5, for which the Al thickness was slightly increased to 10 nm. We now notice a knee-like structure just above the gap voltage, which is caused by the proximity effect of the bottom Nb-electrode in the metallic aluminium, but the manifestation of this knee can still be called small. The subgap behaviour, on the other hand, is significantly improved, indicating an overall better surface coverage of the bottom Nb-electrode and a less “leaky” tunnel barrier. This also suggests that increasing the Al thickness even slightly further, one should find an optimum for which the leakage of quasi-particles is low enough while suppressing the proximity effect as much as possible. We therefore will not discuss the full characterisation of these first fabricated wafers here but instead present the characterisation of CrossJJs fabricated with the optimal parameters for tri-layer deposition, which were part of wafer CrossJJ4w13v3.

4.2 Josephson Tunnel Junctions With 14 nm Aluminium

We now present the quality analysis of some of the Josephson junctions that were produced on the wafer CrossJJ4w13v3. For this, we analyse the quality parameters extracted from the *IV*- characteristics, as discussed in section 2.3. Generally, the yield of functioning junctions for each wafer was around 96% but this wafer was chosen due to the yield of very high quality parameters. The wafer CrossJJ4w13v3 has a tri-layer that consists of 100 nm Nb in both, top and bottom layer, and a 14 nm thick Al layer that was oxidised in an oxygen atmosphere of $p_{\text{ox}} = 33.33 \text{ mbar}$ for $t_{\text{ox}} = 15 \text{ min}$. Figure 4.3 shows a typical *IV*- characteristics of a cross-type Josephson junction with an area of $A = 1 \mu\text{m} \times 1 \mu\text{m}$ at $T = 4.2 \text{ K}$. One can immediately learn

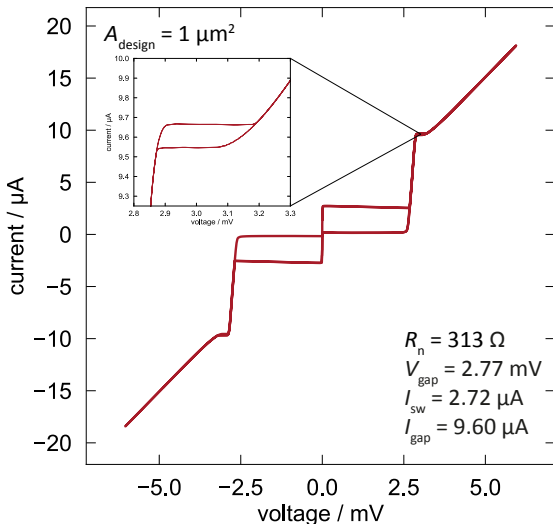


Figure 4.3: *IV*- characteristics of a CrossJJ of wafer CrossJJ4w13v3 with $A_{\text{design}} = 1 \mu\text{m} \times 1 \mu\text{m}$ measured at $T = 4.2 \text{ K}$. A zoom-in onto the artifact caused by the proximity effect is also provided. The qualitative structure is close to what one would expect in theory, indicating the successful fabrication of a high quality JJ down to this small size of $1 \mu\text{m}^2$. The subgap area and the switching current are well defined without any voltage-dependent slope. The critical current agrees with what we expect for that JJ area, given the oxidation parameter and thus the critical current density.

from the qualitative structure that this is a junction of high quality, which is backed up by the very low leakage of quasi-particles in the subgap area. Nonetheless, the gap voltage with $V_{\text{gap}} = 2.77 \text{ mV}$ is roughly 2% less than the expected lower bound of 2.83 mV to 2.93 mV and a proximity-knee in form of a step between the gap voltage and the ohmic behaviour can also be seen. The slightly lower gap voltage can be explained by the proximity effect of the residual non-oxidised Al which lies inbetween the bottom Nb-electrode and the insulating AlO_x barrier, reducing the gap energy to break up Cooper pairs in the bottom electrode. This is most likely due to the thickness of the sputtered Al, which could not be thoroughly oxidised leaving a residual layer of Al between the bottom electrode and the oxide layer.

In order to analyse JJ-area-dependent quantities like the normal state resistance $R_n = \rho_n / A$ as well as the critical current $I_c = j_c A$ and its related quantity, the gap current $I_{\text{gap}} = I_c / \kappa = j_{\text{gap}} A$, we need to consider that the designed area for the junction is not necessarily the same as the fabricated one due to the tolerances and a possible bias of the photolithographic steps or of the etching from the side of the wet-chemical etching of the Al layer or due to the tolerances or bias of the anisotropic ICP-RIE dry etching process.

We can extract this average offset ΔW of the side length of a JJ by determining the zero point of the linear fits $I_c(A_{\text{design}})$ and $R_n(1/A_{\text{design}})$ and requiring that for vanishing arguments x of both functions y , the value of the functions is also zero.

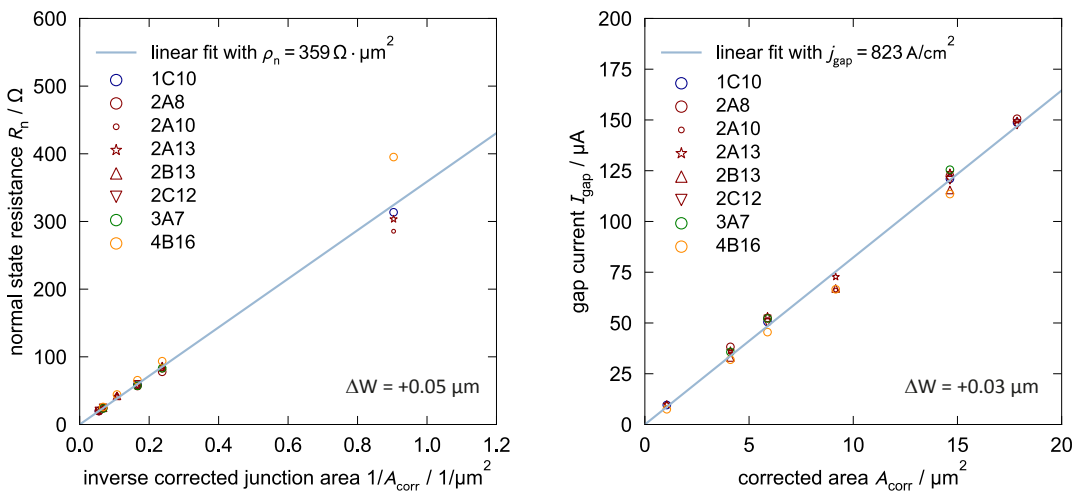


Figure 4.4: Linear fits to the normal state resistance R_n and gap currents and the respectively applied correction for the JJ side length ΔW . Left: Normal state resistance R_n plotted against the inverse corrected junction area $1/A_{\text{corr}}$. The corresponding linear fit determines the normal state resistivity $\rho_n = 359 \Omega \mu\text{m}^2$. Right: Gap current I_{gap} plotted against the corrected area A_{corr} . The corresponding linear fit determines the gap current density $j_c = 823 \text{ A}/\text{cm}^2$.

The offset Δx for $y = 0$ corresponds to ΔA and ΔW is determined by taking the square root, assuming that the CrossJJ areas are quadratic: $\Delta W = \sqrt{\Delta A}$. We can plot the extracted normal state resistances against the inverse of the corrected areas $A_{\text{corr}} = (W_{\text{design}} + \Delta W)^2$, for which we then can fit a linearly dependent function through the origin given by

$$R_n = \frac{\rho_n}{(W_{\text{design}} + \Delta W)^2} \quad (4.1)$$

with the parameters ΔW , the average offset of the side length of a JJ, and ρ_n , the normal state resistivity. The data in Figure 4.4 assumes the average side length correction to be $\Delta W = 0.05 \mu\text{m}$ for the ρ_n -fit. The side length of the quadratic JJ seems to be on average slightly larger than designed. One can see how well the resistance scales linearly with the inverse corrected area. Since also the gap current depends on the area, one can alternatively plot the gap current against the corrected JJ area and fit the function

$$I_{\text{gap}} = j_{\text{gap}}(W_{\text{design}} + \Delta W)^2 \quad (4.2)$$

with the the gap current density j_{gap} . The data in Figure 4.4 assumes the average side length correction to be $\Delta W = 0.03 \mu\text{m}$. Again we can see the expected linear behaviour of the gap current against the corrected area. The side length correction, based on the assumption of an uniform deviation on wafer-scale, results for both fits

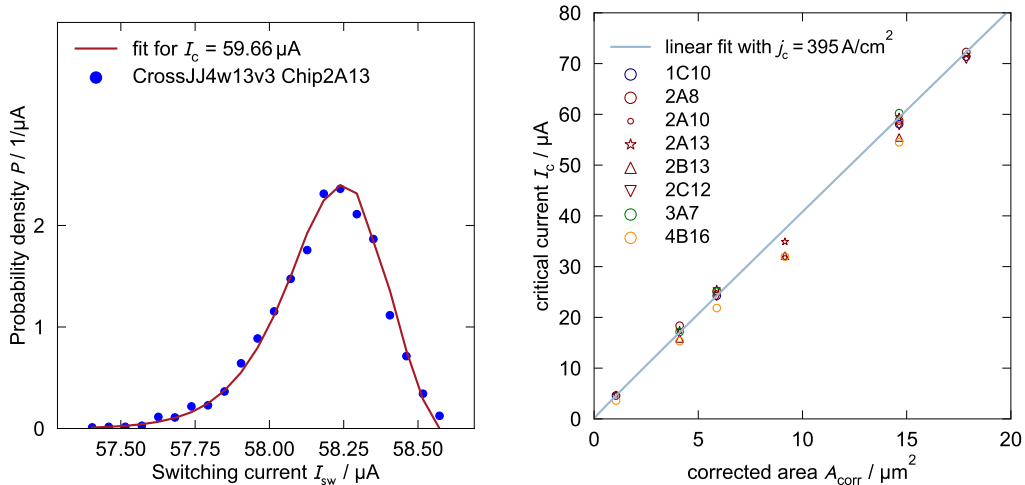


Figure 4.5: Left: measured probability density $P(I_{\text{sw}})$ of a CrossJJ of chip 2A13 of wafer CrossJJ4w13v3 with $A_{\text{design}} = 3.8 \mu\text{m} \times 3.8 \mu\text{m}$ and corresponding fit of a Poisson distribution to determine the critical current I_c . Right: Critical current I_c plotted against the corrected area using the determined factor $\kappa = I_c/I_{\text{gap}} = 0.48$ and the linear fit to determine the critical current density j_c .

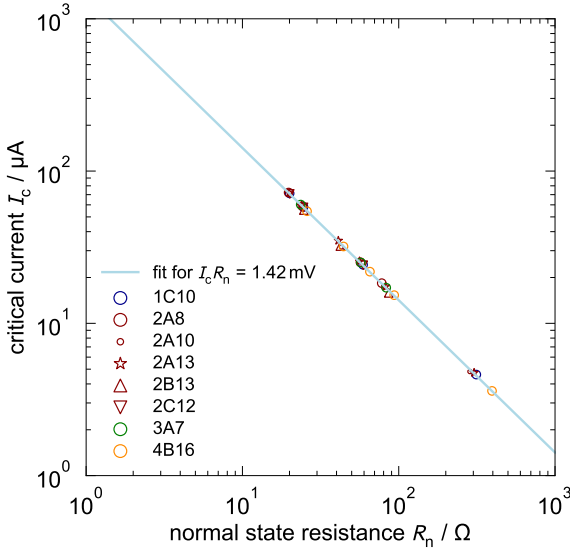


Figure 4.6: Critical current I_c plotted against the normal state resistance R_n and the corresponding fit to determine the $I_c R_n$ product.

in two very similar values. The discrepancy between the two fits might be reduced by having more CrossJJs measured since the deviation itself is already small. Even for the smallest CrossJJs, which have a side length of only $1 \mu\text{m}$, $\Delta W/W$ is only 5%. The difference between the determined side length corrections is also on the same scale as the difference of the determined deviations which have been found in a previous work of this research group [Bau22]. How the critical current behaves in dependence of the junction area can be determined by converting the gap current into the critical current with the factor κ for which we found an average value of 0.48. This prefactor was determined, as described in subsection 3.3.2, by fitting a Poisson distribution to the distribution $P(I_{\text{sw}})$ of the switching currents, as seen in Figure 4.5 for a $3 \mu\text{m} \times 3 \mu\text{m}$ CrossJJ. The same analysis was also done for a handful of larger CrossJJs of chips from different areas of the wafer and then averaged. This way we are able to plot the corrected critical current against the corrected area and fit the function

$$I_c = j_c(W_{\text{design}} + \Delta W)^2 \quad (4.3)$$

to determine the critical current density j_c as well. That resulted in a critical current density of $j_c = 395 \text{ A/cm}^2$ with a convincingly linear behaviour.

Having determined the critical current, we are able to plot the normal state resistance versus the critical current. This is shown in the Figure 4.6 for which we fitted the function $R_n = a/I_c$ with the fit parameter a that corresponds to the quality parameter $I_c R_n$ and yielded a value of 1.42 mV. The $I_c R_n$ product can be also determined by the previously fitted values for the resistivity and critical current density which results in the same value of 1.42 mV. Although these values are basically the same if rounded to two decimal places, both of them lie very distant to the theoretical value of 2.06 mV given by the Ambegaokar-Baratoff theory for a gap voltage of

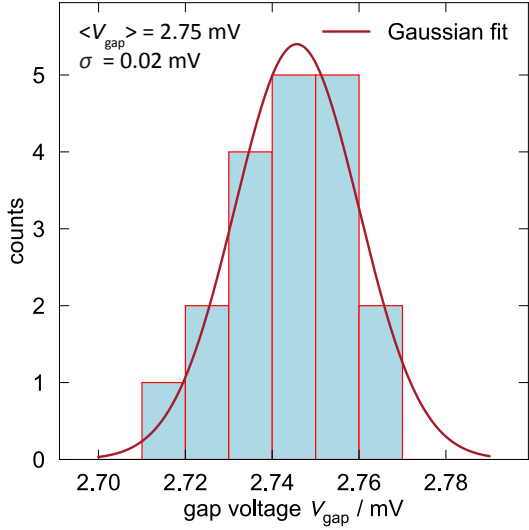


Figure 4.7: Histogram of the gap voltages of all measured CrossJJs of wafer CrossJJ4w13v3. The mean value $\langle V_{\text{gap}} \rangle$ as well as the standard deviation σ were determined by fitting a Gaussian function to it.

2.75 mV. The discrepancy might be explained by the fact that this theory is based on Cooper-pair tunneling through a single, well-defined insulating barrier and does not consider the additional layer of metallic aluminium with lower T_c and proximity effects.

Furthermore, we plotted the gap voltage in form of a histogram to show the mean value and spread of values on wafer-scale. The same could be done for the resistance ratio R_{sg}/R_n but as already mentioned previously, this was skipped for this particular wafer due to the high subgap resistance which is larger than the limiting resistor on the driven current side of our voltage measurement. It influenced the current ramp and thus results in an overestimation of the subgap resistance.

Figure 4.7 shows the histogram of gap voltages and depicts a very small parameter spread of 0.02 mV for the gap voltage, which is another indicator of the uniformity and homogeneity of CrossJJs on wafer-scale which were produced with the mentioned parameters in the framework of this thesis.

4.3 Estimating the Capacitance of Josephson Junctions

As described in section 2.5, using the experimental setup shown in Figure 3.8, we are able to estimate the capacitance of the fabricated JJs by utilising the LC -resonances of unshunted dc-SQUIDs. On the left of Figure 4.8, an optical microscope picture of an unshunted dc-SQUID is shown, which was fabricated within the framework of this thesis.

For this capacitance estimation, in addition to the setup of recording the IV -characteristics of the JJ, we apply a homogeneous magnetic field via a Helmholtz coil, with the chip lying in the centre of the Helmholtz coil geometry such that a homogeneous magnet-

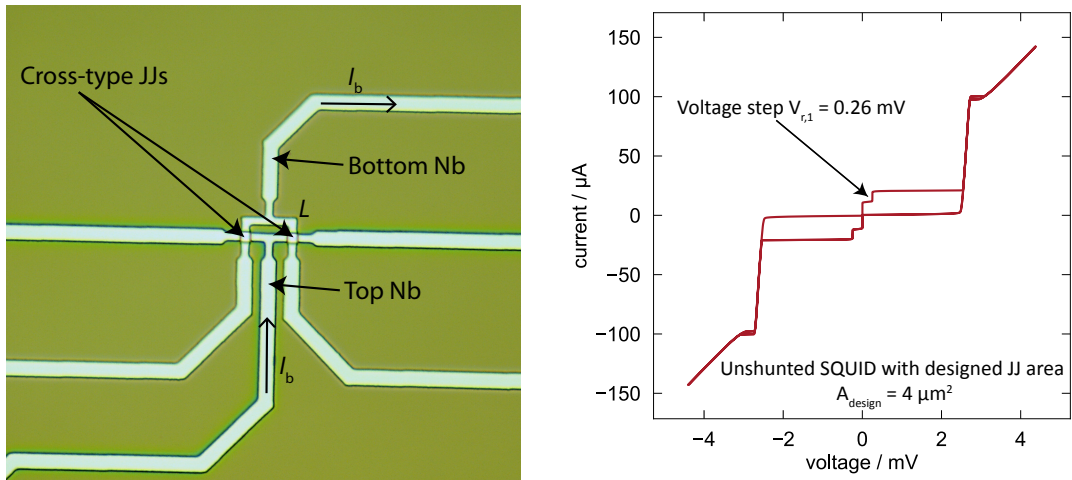


Figure 4.8: Left: Optical microscope picture of an unshunted dc-SQUID. For the capacitance estimation, a bias current signal I_b is driven through the dc-SQUID with an inductance L , while a magnetic flux is applied by a Helmholtz coil. Right: IV -characteristics of an unshunted dc-SQUID of the wafer CrossJJ4w13v3 based on cross-type JJs with $A_{\text{design}} = 2 \mu\text{m} \times 2 \mu\text{m}$ and loop design as seen on the left, measured at $T = 4.2 \text{ K}$. The applied magnetic flux was around $\Phi_0/2$.

ic field is applied. Applying a magnetic field such that we have a flux Φ threading the SQUID, which is around $\Phi = (n + 1/2)\Phi_0$ so that the maximal supercurrent is suppressed enough to make a Shapiro step, i.e. a voltage step, visible, led to the results shown in Figure 4.8 on the right. In order to determine the capacitance, we additionally need the inductance of the SQUID loop. For this, we numerically estimate the inductance L by using approximations under the assumption of idealized polygonal superconducting structures [Wol17]. This yielded a value of $L = 8.0 \text{ pH}$. It is important to note that this estimation does not take the kinetic inductance of niobium into consideration and assumes ideal superconductors. Using Equation 2.76, we find a specific capacitance of the JJ of $C'_{\text{JJ}} \approx 10 \mu\text{F}/\text{cm}^2$ for $j_c = 395 \text{ A}/\text{cm}^2$. Comparing this to the measurement results of [Bau22], which found $C'_{\text{JJ}} \approx 6.5 \mu\text{F}/\text{cm}^2$ for $j_c = 395 \text{ A}/\text{cm}^2$, our CrossJJs only have a slightly larger capacitance. Since our approximation of the inductance did not include the contribution of the kinetic inductance of the inductor material, which also varies for the same material depending on the facility used to fabricate it, a direct quantitative comparison to the measurement results of [Bau22] should be treated with caution.

A more reliable way of determining the junction capacitance is described in [Bau22], which created a flux by applying an additional control current I_{ctr} in the SQUID itself by utilising all different parts of the SQUID loop inductance. The period of the modulation of the maximal supercurrent is then depending on the inductance L of

the driven part of the SQUID loop and can therefore be determined experimentally, which includes the contribution due to the kinetic inductance of the niobium material.

5. Summary and Outlook

Superconducting quantum interference devices (SQUIDs) represent the state-of-the-art technology for precision measurement detectors of magnetic field changes with high bandwidth and are used in many applications in which particularly small electrical signals are to be read out with a sensitivity close to the quantum limit. In our group, SQUIDs are used for the read-out of tens and hundreds of metallic magnetic calorimeters (MMCs) as well as for the detailed investigation of superconducting quantum circuits. In order to guarantee a reliable read-out of detectors without degradation of the energy resolution of the MMCs themselves, it is of particular interest to optimise the dc-SQUIDs fabricated in our group for those applications. Since the properties of the dc-SQUID strongly depend on its core element, the Josephson junction, it is of great importance to achieve a reliable production of high quality JJs minimising inhomogeneities on wafer-scale as well as parasitic effects impeding its performance.

Within the framework of this thesis, the Nb/Al-AlO_x/Nb tri-layer deposition, which defines the Josephson tunneling contact, was optimised in a new PreVAC sputtering system by adjusting sputtering parameters like the power of the sputtering source and the pressure of the Ar process gas. This was done in order to find a point in parameter space such that the 100 nm thick Nb films grow with superconducting properties close to bulk Nb and satisfactory surface properties for the deposition of further layers. For this we recorded the stress on the thermally oxidised Si-substrate as well as the critical temperature T_c of the grown films. The subsequent sputtering of Al as precursor of the tunnel barrier was varied in thickness to investigate the effects on the quality parameters of the cross-type Josephson junctions. The successful investigation and optimisation of these fabrication steps discussed in this thesis will help to ramp up the production of high quality cross-type Josephson-junction-based dc-SQUIDs and finalize the steps in completely migrating from the window-type based fabrication to the cross-type based one and make use of the advantages it brings along.

The most critical fabrication step for the quality of the junction-defining tri-layer depends on how the Al film grows on the bottom Nb-electrode. During the deposition of Al, it seems like the Al atoms diffuse into the pits of the Nb surface such that it smooths out the potentially uneven Nb surface. If this surface has too many high peaks or deep pits, which is the case for strongly tensile or compressively stressed films, parts of the bottom Nb may remain uncovered and cause the appearance of pinholes increasing the subgap leakage of a Josephson junction. We therefore ad-

justed the sputtering parameters such that the grown Nb films would only apply a slightly compressive stress onto the substrate. This was done by measuring the substrates curvature before and after deposition as well as utilising the bending plate method to calculate the applied stress onto the substrate. With this method we were able to successfully minimize the applied stress of the grown Nb films for 200 nm and 100 nm thick films. For 200 nm thick films we managed to decrease the average compressive stress by at least a factor of 5 to $\sigma = -79 \text{ MPa}$.

The thickness of the Al layer determines not only how well the surface of the bottom electrode is covered, it also determines the strength of the proximity effect. Therefore, a compromise value for the thickness, taking both effects into account, had to be found. The oxidation parameters for the Al layers were chosen to be $p_{\text{ox}} t_{\text{ox}} = 2.97 \cdot 10^6 \text{ Pa} \cdot \text{s}$, the same as in the previously used sputtering system. The direct comparison revealed that the resulting critical current density of $j_c = 395 \text{ A/cm}^2$ is very close to the values one achieved in the previously used sputtering system, as seen in Figure 3.7. Nonetheless, one needs further points to make more viable statements regarding the behaviour of the critical current density in terms of the oxidation parameters. These steps are what led to the fabrication of a CrossJJ wafer with high quality JJs that have been fabricated for the first time in the new sputtering system.

After the discussed optimization steps, we were able to fabricate a wafer with high quality cross-type based Josephson junctions with homogeneously distributed quality parameters on wafer-scale. With a yield of more than 96 % we were able to fabricate CrossJJs down to a designed area of $1 \mu\text{m}^2$ with the side length of fabricated junctions deviating by only $\sim 0.05 \mu\text{m}$ from the design. Measuring the *IV*-characteristics of the JJs at $T = 4.2 \text{ K}$ we were even able to correct the data on the critical current as derived at finite temperature using the method previously introduced in this group to find out the critical current in the $T \rightarrow 0$ limit. Furthermore, we were able to estimate the CrossJJs capacitance by utilising the *LC*-resonance of unshunted dc-SQUIDs and measuring the resulting Shapiro steps. However, we note again that this estimation is very rough due to the fact of neglecting the kinetic inductance of the deposition dependent Nb material. Because of this, a more reliable method would be the measuring of resonance curves while applying control currents through parts of the SQUID due to the additional benefit of measuring the inductance of the structured material.

In a continuation of this thesis, one could further investigate the superconducting properties of the films sputtered in the PreVAC sputtering system by additionally measuring the Fraunhofer pattern of the critical current density profile of the Josephson junction and determining the magnetic penetration depth of the superconducting material. It is also of interest to analyse the surface structure of the AlO_x by utilising atomic force microscopy for instance to get a further understanding of

the confocally sputtered Al films. Furthermore, more combinations of Ar pressure during Nb sputtering and Al thickness should be tested to reduce the proximity effect even further while keeping the same high quality *IV*-characteristics structure. Here, one can also vary the angle of the Al sputtering gun and further characterize how the confocal sputtering geometry influences the surface coverage of the bottom electrode. With the arrival of a new laserlithograph for the Kirchhoff-Institute of Physics in the upcoming months, which is able to reliably produce photomask structures down to sizes of 500 nm, one is able to produce even smaller CrossJJs and investigate the possible challenges that might come up in fabricating those. Having established a reliable fabrication of high quality cross-type based JJs, the next step would be to produce cross-type JJ-based dc-SQUIDs in the PreVAC sputtering system and utilise the advantages of a smaller intrinsic capacitance, such as increasing the shunt resistance to hold the Steward-McCumber parameter at the same value thus increasing the characteristic voltage and reduce thermal noise. Further work in optimising these dc-SQUIDs in terms of noise can be done by looking into new designs for thermalising certain shunt elements of the dc-SQUID circuit. As such, the optimisation steps conducted in the framework of this thesis shall build a basis for further research and optimisation of cross-type based dc-SQUIDs, such that they become the new standard in our group and possibly worldwide in the context of SQUIDs and superconducting electronics at the quantum limit in general.

I. Appendix

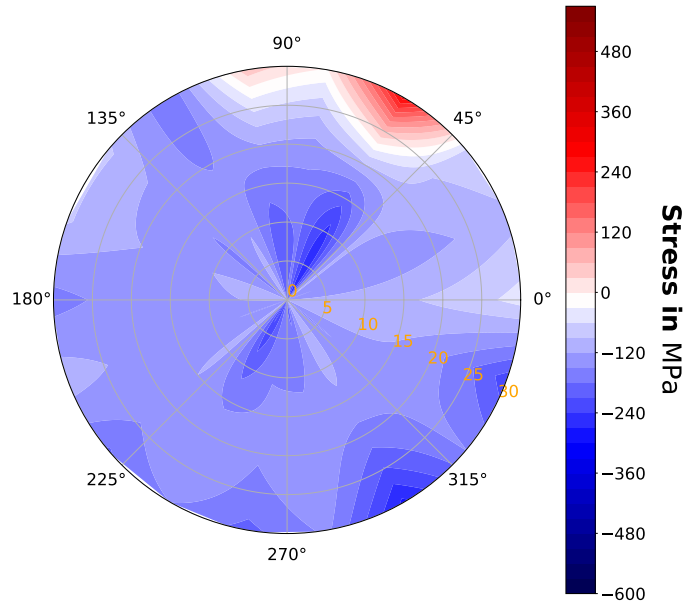


Figure I.1: 2D Stress map of part of a 3inch Si-Wafer with 100 nm Nb deposited on it. The sputter parameters were: Ar pressure $p = 4 \mu\text{bar}$, sputtering source power $P = 700 \text{ W}$. The orange ticks show the radial distance from the middle in mm. Negative stress values (blue) showcase compressive stress while positive stress values (red) showcase tensile stress. The stress up to a radius of $r = 20 \text{ mm}$ averages to $\sigma = -(141 \pm 36) \text{ MPa}$.

Wafer name	Al thickness [nm]	p_{ox} [mbar]	t_{ox} [min]	Ar pressure [μbar]
CrossJJ4w13v1	7	33.33	15	7
CrossJJ4w13v2	7	100.00	15	7
CrossJJ4w13v3	14	33.33	15	7
CrossJJ4w13v4	10	33.33	15	4
CrossJJ4w13v5	10	33.33	15	4

Table I.1: Overview of the fabrication parameters for wafers containing cross-type JJs produced within the framework of this thesis. The Ar pressure indicates the pressure of the process gas during sputtering. The last two characters of the wafer name indicate the version number. After fabrication of CrossJJ4w13v3 the sputter chamber was opened for maintenance purposes and the Al target moved to a different magnetron sputter gun with a higher range for angle movement. CrossJJ4w13v4 was scrapped since the fabrication was conducted without prior erosion of the oxidised layer of the targets. CrossJJ4w13v5, as a second attempt of version 4, was fabricated after ensuring that the oxide layer of the targets was eroded.

Bibliography

- [Alp15] B. Alpert, M. Balata, D. Bennett, M. Biasotti, C. Boragno, C. Brofferio, V. Ceriale, D. Corsini, P. K. Day, M. De Gerone, R. Dressler, M. Faverzani, E. Ferri, J. Fowler, F. Gatti, A. Giachero, J. Hays-Wehle, S. Heinitz, G. Hilton, U. Köster, M. Lusignoli, M. Maino, J. Mates, S. Nisi, R. Nizzolo, A. Nucciotti, G. Pessina, G. Pizzigoni, A. Puiu, S. Ragazzi, C. Reintsema, M. Ribeiro Gomes, D. Schmidt, D. Schumann, M. Sisti, D. Swetz, F. Terranova, and J. Ullom, HOLMES, *The European Physical Journal C*, **75**(3), 2015.
- [Amb63] V. Ambegaokar and A. Baratoff, Tunneling Between Superconductors, *Physical Review Letters*, **10**(11), 486–489, 1963.
- [Bar57a] J. Bardeen, L. N. Cooper, and J. R. Schrieffer, Microscopic Theory of Superconductivity, *Phys. Rev.*, **106**, 162–164, 1957.
- [Bar57b] J. Bardeen, L. N. Cooper, and J. R. Schrieffer, Theory of Superconductivity, *Phys. Rev.*, **108**(5), 1175–1204, 1957.
- [Bau22] Fabienne Bauer, *Rauscharme Stromsensor-dc-SQUIDs mit Impedanzanpassung für metallische magnetische Kalorimeter*, Dissertation, Kirchhoff-Institut für Physik, Universität Heidelberg, 2022.
- [Bru82] J. J. P. Bruines, V. J. de Waal, and J. E. Mooij, Comment on: “DC SQUID: Noise and optimization” by Tesche and Clarke, *J. Low Temp. Phys.*, **46**, 383–386, 1982.
- [Buc04] W. Buckel and R. Kleiner, *Superconductivity: Fundamentals and Applications*, Wiley-VCH, 2004.
- [Bue83] M. Buettiker, E. P. Harris, and R. Landauer, Thermal activation in extremely underdamped josephson-junction circuits, *Phys. Rev. B*, **28**, 1268–1275, 1983.
- [Can91] R. Cantor, T. Ryhänen, D. Drung, H. Koch, and H. Seppä, Design and optimization of DC SQUIDs fabricated using a simplified four-level process, *IEEE Transactions on Magnetics*, **2**(2), 2927–2931, 1991.
- [Can96] Robin Cantor, *Dc Squids: Design, Optimization and Practical Applications*, 179–233, Springer Netherlands, Dordrecht, 1996.

- [Car90] J. P. Carbotte, Properties of Boson-Exchange Superconductors, *Reviews of Modern Physics*, **62**(4), 1027–1157, 1990.
- [Cas96] Maria Castellano, Roberto Leoni, Guido Torrioli, Fabio Chiarello, C. Cosmelli, A. Costantini, G. Diambrini Palazzi, Pasquale Carelli, Roberto Cristiano, and L. Frunzio, Switching dynamics of nb/alox/nb josephson junctions: Measurements for an experiment of macroscopic quantum coherence, *Journal of Applied Physics*, **80**, 2922 – 2928, 1996.
- [Cla88] J. Clarke and R. Koch, The Impact of High Temperature Superconductivity on SQUIDs, *Science*, **242**, 217–223, 1988.
- [Cla04] J. Clarke and A. I. Braginski (Ed.), *The SQUID Handbook: Vol. 1, Fundamentals and Technology of SQUIDs and SQUID Systems*, Wiley-VCH, 2004.
- [Coo56] L. N. Cooper, Bound Electron Pairs in a Degenerate Fermi Gas, *Phys. Rev.*, **104**, 1189–1190, 1956.
- [Coo65] D. D. Coon and M. D. Fiske, Josephson ac and Step Structure in the Supercurrent Tunneling Characteristic, *Physical Review*, **138**(3A), A744–A746, 1965.
- [Dev85] Michel H. Devoret, John M. Martinis, and John Clarke, Measurements of macroscopic quantum tunneling out of the zero-voltage state of a current-biased josephson junction, *Phys. Rev. Lett.*, **55**, 1908–1911, 1985.
- [Dev07] Aditya Devalapalli, 2007.
- [Dru11] D. Drung, J. Beyer, J.-H. Storm, M. Peters, and T. Schurig, Investigation of Low-Frequency Excess Flux Noise in DC SQUIDs at mK Temperatures, *IEEE T. Appl. Supercon.*, **21**, 340–344, 2011.
- [Du07a] J. Du, A. D. M. Charles, and K. D. Petersson, Study of the Surface Morphology of Nb Films and the Microstructure of Nb/AlO_x-Al/Nb Trilayers, *IEEE Transactions on Applied Superconductivity*, **17**(2), 3520–3524, 2007.
- [Du07b] J. Du, A. D. M. Charles, K. D. Petersson, and E. W. Preston, Influence of Nb film surface morphology on the sub-gap leakage characteristics of Nb/AlO_x-Al/Nb Josephson junctions, *Superconductor Science and Technology*, **20**(11), S350–S355, 2007.
- [Fey64] R. P. Feynman, R. B. Leighton, and M. Sands, *The Feynman Lectures on Physics*, Addison-Wesley, 1964.

- [Fle05] A. Fleischmann, C. Enss, and G. Seidel, *Cryogenic Particle Detection*, Volumen 99 in *Topics in applied physics*, Kapitel Metallic Magnetic Calorimeters, 149–215, Springer-Verlag Berlin Heidelberg, 2005.
- [Ful72] T. A. Fulton, L. N. Dunkleberger, and R. C. Dynes, Quantum Interference Properties of Double Josephson Junctions, *Phys. Rev. B*, **6**, 855–875, 1972.
- [Gas17] L. Gastaldo, K. Blaum, K. Chrysalidis, T. Day Goodacre, A. Domula, M. Door, H. Dorrer, Ch. E. Düllmann, K. Eberhardt, S. Eliseev, C. Enss, A. Faessler, P. Filianin, A. Fleischmann, D. Fonnesu, L. Gamer, R. Haas, C. Hassel, D. Hengstler, J. Jochum, K. Johnston, U. Kebschull, S. Kempf, T. Kieck, U. Köster, S. Lahiri, M. Maiti, F. Mantegazzini, B. Marsh, P. Neroutsos, Yu. N. Novikov, P. C. O. Ranitzsch, S. Rothe, A. Rischka, A. Saenz, O. Sander, F. Schneider, S. Scholl, R. X. Schüssler, Ch. Schweiger, F. Simkovic, T. Stora, Z. Szücs, A. Türler, M. Veinhard, M. Weber, M. Wegner, K. Wendt, and K. Zuber, The electron capture in ^{163}Ho experiment – ECHO, *The European Physical Journal Special Topics*, **226**(8), 1623–1694, 2017.
- [Gin50] V. L. Ginzburg and L. Landau, On the theory of superconductivity, *Zh. Èksper. Teoret. Fiz.*, **20**, 1064–1082, 1950.
- [Gor34] C Jo Gorter and H Casimir, The thermodynamics of the superconducting state, *Z. tech. Phys.*, **15**, 539–42, 1934.
- [Hen17] Daniel Hengstler, *Development and characterization of two-dimensional metallic magnetic calorimeter arrays for the high-resolution X-ray spectroscopy*, Dissertation, Kirchhoff-Institut für Physik, Universität Heidelberg, 2017.
- [Ima92a] T. Imamura and S. Hasuo, Fabrication of high quality Nb/AlO_x-Al/Nb Josephson junctions: II - Deposition of Thin Al Layers on Nb Films, *IEEE Transactions on Applied Superconductivity*, **2**(2), 84–94, 1992.
- [Ima92b] T. Imamura, T. Shiota, and S. Hasuo, Fabrication of high quality Nb/AlO_x-Al/Nb Josephson junctions: I - Sputtered Nb films for junction electrodes, *IEEE Transactions on Applied Superconductivity*, **2**(1), 1–14, 1992.
- [Jac66] R.J Jaccodine and WA Schlegel, Measurement of strains at si-sio2 interface, *Journal of Applied Physics*, **37**(6), 2429–2434, 1966.
- [Jak21] Christopher Jakob, *Magnetfeldabhängige Messungen der charakteristischen Eigenschaften von Nb/Al-AlOx/Nb-Josephson-Kontakten*, Diplomarbeit, Kirchhoff-Institut für Physik, Universität Heidelberg, 2021.

- [Jen67] FA Jenkins and HE White, *Fundamentals of Optics*, McGraw-Hill, 1967.
- [Joh28] J. B. Johnson, Thermal Agitation of Electricity in Conductors, *Phys. Rev.*, **32**(1), 97–109, 1928.
- [Jos62] B. D. Josephson, Possible new effects in superconductive tunnelling, *Physics Letters*, **1**(7), 251–253, 1962.
- [Jos65] B. D. Josephson, Supercurrents through barriers, *Advances in Physics*, **14**(56), 419–451, 1965.
- [Kem13] S. Kempf, A. Ferring, A. Fleischmann, L. Gastaldo, and C. Enss, Characterization of the reliability and uniformity of an anodization-free fabrication process for high-quality Nb/Al-AlO_x/Nb Josephson junctions, *Superconductor Science and Technology*, **26**(6), 065012, 2013.
- [Kem18] S. Kempf, A. Fleischmann, L. Gastaldo, and C. Enss, Physics and Applications of Metallic Magnetic Calorimeters, *Journal of Low Temperature Physics*, 1–15, 2018.
- [Kra40] H.A. Kramers, Brownian motion in a field of force and the diffusion model of chemical reactions, *Physica*, **7**(4), 284–304, 1940.
- [Lan80] L.D. Landau, E.M. Lifshitz, and L.P. Pitaevskii, *Course of Theoretical Physics: Statistical Physics, Part 2 : by E.M. Lifshitz and L.P. Pitaevskii*, Number Bd. 9, 1980.
- [Lik79] K. K. Likharev, Superconducting weak links, *Rev. Mod. Phys.*, **51**, 101–159, 1979.
- [Lik86] K. K. Likharev, *Dynamics of Josephson Junctions and Circuits*, Gordon and Breach, New York, 1986.
- [Lon50] F. London, *Superfluids*, Structure of matter series, Wiley, New York, 1950.
- [Mae95] M. Maezawa, M. Aoyagi, H. Nakagawa, I. Kurosawa, and S. Takada, Specific capacitance of Nb/AlO_x/Nb Josephson junctions with critical current densities in the range of 0.1 – 18 kA/cm², *Applied Physics Letters*, **66**(16), 2134–2136, 1995.
- [Mag81] J. H. Magerlein, Specific capacitance of Josephson tunnel junctions, *IEEE Transactions on Magnetics*, **17**(1), 286–289, 1981.
- [McC68] D. E. McCumber, Effect of ac Impedance on dc Voltage-Current Characteristics of Superconductor Weak-Link Junctions, *Journal of Applied Physics*, **39**(7), 3113–3118, 1968.

- [Mei33] W. Meissner and R. Ochsenfeld, Ein neuer Effekt bei Eintritt der Supraleitfähigkeit, *Naturwissenschaften*, **21**(44), 787–788, 1933.
- [Nyq28] H. Nyquist, Thermal Agitation of Electric Charge in Conductors, *Phys. Rev.*, **32**(1), 110–113, 1928.
- [Onn11] H. Kamerlingh Onnes, The Superconductivity of Mercury, *Comm. Phys. Lab. Univ. Leiden*, **122**, **124**, 1911.
- [Ryh89] Tapani Ryhänen, Heikki Seppä, Risto Ilmoniemi, and Jukka Knuutila, Squid magnetometers for low-frequency applications, *Journal of Low Temperature Physics*, **76**, 287–386, 1989.
- [Sch63] J. R. Schrieffer and J. W. Wilkins, Two-Particle Tunneling Processes between Superconductors, *Phys. Rev. Lett.*, **10**, 17–20, 1963.
- [Sha63] Sidney Shapiro, Josephson currents in superconducting tunneling: The effect of microwaves and other observations, *Phys. Rev. Lett.*, **11**, 80–82, 1963.
- [Sha64] Sidney Shapiro, Andre R. Janus, and Sandor Holly, Effect of microwaves on josephson currents in superconducting tunneling, *Rev. Mod. Phys.*, **36**, 223–225, 1964.
- [Sil88] Paolo Silvestrini, Sergio Pagano, Roberto Cristiano, O. Liengme, and K. E. Gray, Effect of dissipation on thermal activation in an underdamped josephson junction: First evidence of a transition between different damping regimes, *Phys. Rev. Lett.*, **60**, 844–847, 1988.
- [Sto09] George Gerald Stoney, The tension of metallic films deposited by electrolysis, *Proceedings of The Royal Society A: Mathematical, Physical and Engineering Sciences*, **82**, 172–175, 1909.
- [Tes77] C. D. Tesche and J. Clarke, dc SQUID: Noise and Optimization, *Journal of Low Temperature Physics*, **294**(3), 1–9, 1977.
- [Tie21] Eite Tiesinga, Peter J. Mohr, David B. Newell, and Barry N. Taylor, Codata recommended values of the fundamental physical constants: 2018, *Rev. Mod. Phys.*, **93**, 025010, 2021.
- [Tsu93] K. Tsukada, J. Kawai, G. Uehara, and H. Kado, Relationship of nb surface morphology and al coverage to the intrinsic stress of magnetron-sputtered nb films, *IEEE Transactions on Applied Superconductivity*, **3**(1), 2944–2946, 1993.

- [Waa84] V. J. de Waal, P. Schrijner, and R. Llurba, Simulation and optimization of a dc SQUID with finite capacitance, *J. Low Temp. Phys.*, **54**(3-4), 215–232, 1984.
- [Wal03] Andreas Wallraff, A. Lukashenko, C. Coqui, Alexander Kemp, Timothy Duty, and AV Ustinov, Switching current measurements of large area josephson tunnel junctions, *Review of Scientific Instruments*, **74**, 2003.
- [WE96] H. Weinstock (Ed.), Squid sensors: Fundamentals, fabrication and applications, 1996.
- [Wei69] M. Weihnacht, Influence of Film Thickness on D. C. Josephson Current, *Phys. Stat. Sol. B*, **32**(2), K169–K172, 1969.
- [Wel94] F. C. Wellstood, C. Urbina, and John Clarke, Hot-electron effects in metals, *Phys. Rev. B*, **49**, 5942–5955, 1994.
- [Wol17] Edward Wolf, Gerald Arnold, Michael Gurvitch, and John Zasadzinski (Ed.), *Josephson Junctions / History, Devices, and Applications*, Jenny Stanford Publishing, 2017.
- [Zim18] F. Zimmerer, *Beurteilung der Qualität von Nb/Al-AlO_x/Nb-Josephson-Kontakten und Charakterisierung des Herstellungsprozesses von Nb/Al-AlO_x/Nb-Dreischichtstrukturen*, Bachelorarbeit, Kirchhoff-Institut für Physik, Universität Heidelberg, 2018.

Ich versichere, dass ich diese Arbeit selbstständig verfasst und keine anderen als die angegebenen Quellen und Hilfsmittel benutzt habe.

Heidelberg, den 01. Juni 2023

.....

(Alexander Stoll)